

1 **Can we use precipitation isotope outputs of Isotopic General Circulation Models to**
2 **improve hydrological modeling in large mountainous catchments on the Tibetan Plateau?**

3

4 Yi Nan¹, Zihua He², Fuqiang Tian¹, Zhongwang Wei³, Lide Tian⁴

5 ¹ Department of Hydraulic Engineering, State Key Laboratory of Hydrosience and Engineering,
6 Tsinghua University, Beijing 100084, China

7 ² Center for Hydrology, University of Saskatchewan, Saskatchewan, Canada

8 ³ Guangdong Province Key Laboratory for Climate Change and Natural Disaster Studies, School of
9 Atmospheric Sciences, Sun Yat-sen University, Guangzhou, Guangdong, China

10 ⁴ Institute of International Rivers and Eco-security, Yunnan University, Kunming, China

11 ***Corresponding to:*** Fuqiang Tian

12 Address: Room 330 New Hydraulic Building, Tsinghua University, Beijing 100084, China

13 Email: tianfq@mail.tsinghua.edu.cn

14 _____

15 **Abstract**

16 Issues related to large uncertainty and parameter equifinality have posed big challenges
17 for hydrological modeling in cold regions where runoff generation processes are particularly
18 complicated. Tracer-aided hydrological models that integrate transportation and fractionation
19 processes of water stable isotope are increasingly used to constrain parameter uncertainty and
20 refine the parameterizations of specific hydrological processes in cold regions. However,
21 commonly unavailability of site sampling of spatially distributed precipitation isotope hampers
22 the practical applications of tracer-aided models in large scale catchments. This study, taken the
23 precipitation isotope data (isoGSM) derived from the Isotopic General Circulation Models
24 (iGCM) as an example, explored its utility in driving a tracer-aided hydrological model in the
25 Yarlung Tsangpo River basin (YTR, around 2×10^5 km² with mean elevation of 4875 m) on the
26 Tibetan Plateau (TP). The isoGSM product was firstly corrected based on the biases between
27 gridded precipitation isotope estimates and limited site sampling measurements. Model
28 simulations driven by the corrected isoGSM data were then compared with those forced by
29 spatially interpolated precipitation isotope from site sampling measurements. Our results
30 indicated that: (1) spatial precipitation isotope derived from the isoGSM data helped to reduce
31 modeling uncertainty and improve parameter identifiability in a large mountainous catchment
32 on the TP, in comparison to a calibration method using discharge and snow cover area fraction
33 without any information of water isotope; (2) model parameters estimated by the corrected
34 isoGSM data presented higher transferability to nested sub-basins and produced higher model
35 performance in the validation period than that estimated by the interpolated precipitation
36 isotope data from site sampling measurements; (3) model calibration forced by the corrected
37 isoGSM data successfully rejected parameter sets that overestimated glacier melt contribution
38 and gave more reliable contributions of runoff components, indicating the corrected isoGSM
39 data served as a better choice to provide informative spatial precipitation isotope than the
40 interpolated data from site sampling measurements at macro scale. This work suggested
41 plausible utility of combining isoGSM data with measurements even from a sparse sampling
42 network in improving hydrological modeling in large high mountain basins.

43 **Key word**

44 Tracer-aided hydrological modeling; Large basins on the Tibetan Plateau; Isotopic General
45 Circulation Models (iGCM) product; iGCM correction with sparse measurements.

46

47 **1. Introduction**

48 Large uncertainty and strong equifinality of parameter calibration are the widely
49 recognized issues in hydrological modelling (Gupta et al., 2008), especially in cold regions
50 where hydrological complexity is highly enhanced by the competitions of multiple water inputs
51 and the strong spatio-temporal variabilities of runoff generation processes (Li et al., 2019).
52 Tracer-aided hydrological models integrating a water or environmental tracer (e.g., stable
53 oxygen isotope, $\delta^{18}\text{O}$) module into the runoff generation architecture have been proved as
54 highly valuable in improving parameter calibration and diagnosing model uncertainty (Son and
55 Sivapalan, 2007; Birkel et al., 2011; Capell et al., 2012; He et al., 2019). Multiple-objective
56 calibration of tracer-aided model towards both runoff and isotope simulation allows for
57 rejection of parameters based on runoff observation alone, consequently makes the model
58 satisfy multiple objectives and reduces the model uncertainty (McGuire et al., 2007). However,
59 practical applications of tracer-aided hydrological modeling are mainly limited in only small to
60 meso scales. The largest basin area where previous tracer-aided modelling has been
61 implemented is around 10^3 km^2 (i.e., Delavau et al., 2017; Campell et al., 2012; Stadnyk et al.,
62 2013). Reasons fall in either the lumped conceptual model structures due to the complicated
63 tracer processes difficult to be coupled with distributed model (Birkel and Soulsby, 2015), or
64 the low availability of tracer data in large basins due to difficulties in the long-term, continuous
65 and high-frequency field sampling works (e.g., Ala-aho et al., 2017; He et al., 2019). The
66 structure and data issues make the model not suitable for capturing the strong spatial variability
67 of hydrological behaviors in large scale basins.

68 The Tibetan Plateau (TP) is the source region of many large rivers (e.g., Brahmaputra,
69 Ganges, Indus, Mekong, among others), which sustain the ecosystems and provide a great
70 proportion of water source for downstream livelihoods and agricultural irrigation (Zhang et al.,
71 2013; Schaner et al., 2012). Decision making of water resource management over TP and its
72 downstream area relies heavily on river runoff in the large basins. Meanwhile, melting water
73 from snow and ice contributes a significant proportion to river runoff in the large basins on TP
74 due to the cold climate and glacier coverage in head watersheds (Li et al., 2019). Runoff in this
75 region is thus highly vulnerable to climate warming. Robust quantification of the contribution
76 of meltwater to river runoff is critical in understanding water resources dynamics on TP
77 (Immerzeel et al., 2013). Although great efforts have been conducted to quantify the
78 contributions of runoff components and their future trends under climate changes on TP (e.g.,
79 Immerzeel et al., 2010; Lutz et al., 2014; Su et al., 2016; Masood et al., 2015), results reported
80 in the wide range of studies show substantial differences (Xu et al., 2019; Tian et al., 2020).
81 The disagreement among studies indicates big challenges on quantifying contributions of runoff

82 components and predicting their future trend in the large basins on TP. The difficulty of this
83 task is mainly related to the large uncertainty of hydrological modelling and parameter
84 calibration in the TP, because of the complex hydrological processes (He et al., 2018) and the
85 commonly inaccurate estimation of precipitation (Xu et al., 2017; He et al. 2017). The strong
86 inter-competitions of runoff processes induced by meltwater versus rainwater and surface water
87 versus subsurface water are inadequately constrained in hydrological models by the commonly
88 used hydrological observation of streamflow (Duethmann et al., 2015), and even additional data
89 of snow/ice coverage (He et al. 2019). Reducing the modelling uncertainty originated from
90 parameter calibration is essential for proper understanding of runoff regimes and robust
91 prediction of future hydrological change.

92 Tracer-aided hydrological models that additionally involve water stable isotope data for
93 parameter calibration have been proved highly capable for constraining the inter-competitions
94 of runoff processes induced by meltwater and rainwater in high mountains (He et al. 2019; Nan
95 et al. 2021), which, however, have not been tested in large basins yet due to the unavailability
96 of precipitation isotope data. Global gridded isotope product potentially serves as an alternative
97 forcing of precipitation isotope data for tracer-aided hydrological models in large basins where
98 high-frequency sampling work in a large region is not feasible. One of these options comes to
99 outputs of the isotopic General or Regional Circulation Models (iGCM and iRCM, Noone and
100 Sturm, 2010; Xi, 2014; Sturm et al., 2005, 2007), which has been proved to have high
101 performance on simulating the seasonal and spatial variations of isotopic signature of
102 precipitation on regional and global scales (Wang et al., 2017; Yao et al., 2013). However, very
103 few works have been conducted to test the behavior of such products on forcing hydrological
104 models. To the best of our knowledge, the only one work was conducted by Delavau et al.
105 (2017), who examined the performance of an iRCM product REMOiso on forcing tracer-aided
106 model in a regional catchment of around 10^3 km² in Canada. Their results indicated that
107 hydrological simulations driven by the iRCM product reproduced the variations of isotopic
108 signature ($\delta^{18}\text{O}$) of river water comparably to the simulations driven by $\delta^{18}\text{O}$ measurements
109 from sampling sites and improved the representations of internal hydrological processes in the
110 model. Those attempts provide sound confidences for exploring the utility of global and
111 regional gridded isotope data products in aiding hydrological modeling in large basins on TP.

112 Motivated by the mentioned backgrounds, we adopted a tracer-aided hydrological model
113 developed by Nan et al. (2021) to simulate runoff processes and the contributions of runoff
114 components to streamflow in a large basin extending around 2×10^5 km² on the TP. The isotope
115 module was driven by two kinds of precipitation isotope data including site measurements from
116 water samples and outputs of iGCM. Scientific questions addressed in this study are two-fold:
117 (1) what are the benefits of involving water isotope data for hydrological modeling in larger
118 catchments? (2) how does the gridded precipitation isotope data of iGCM products perform on

119 forcing tracer-aided hydrological model in large basins?

120 **2. Materials and methodology**

121 **2.1 Study area**

122 The Yarlung Tsangpo River (YTR) located in the southern TP on the north of Himalaya
123 Mountain (Fig. 1) is one of the longest rivers (longer than 2000 km) originating from TP. The
124 YTR basin is located in the range of 27-32°N and 82-97°E, with an elevation range of 2900-
125 6900 m a. s. l. The mean annual precipitation in YTR basin is around 470 mm, which is
126 dominated by South Asian Monsoon in the Indian Ocean hydrosphere-atmosphere system,
127 resulting in obvious wet season from June to September (Dong et al., 2016). Contributing area
128 to the Nuxia hydrological station extends approximately 2×10^5 km², around 2% of which is
129 covered by glacier. Plenty of previous works have shown the great contribution of snow and
130 glacier melting to the runoff in YTR (e.g., Chen et al., 2017; Tian et al., 2020).

131 The Karuxung River (KR) catchment is located in the upper region of YTR basin, on the
132 northern slope of the Himalayan Mountains, which is used for model evaluation in sub-basin
133 because of its high glacierized area proportion (around 20%). The KR originates from the Lejin
134 Jangsan Peak of the Karola Mountain at 7206 m above sea level (a.s.l.), and flows into the
135 Yamdrok Lake at 4550m a.s.l. (Zhang et al., 2006a). The KR catchment covers an area of 286
136 km². Runoff in KR catchment is strongly influenced by the headwater glaciers which cover an
137 area of around 58 km².

138 **[Figure 1]**

139 **2.2 Hydro-meteorological data and site water sampling for isotope analysis**

140 Digital elevation model (DEM) data in the YTR catchment with a spatial resolution of 30-
141 m was extracted from the Geospatial Data Cloud (<http://www.gscloud.cn>). The 3-hour $0.1^\circ \times 0.1^\circ$
142 China Meteorological Forcing Dataset (CMFD) which combined multiple datasets (e.g.,
143 GLDAS and TRMM) with the national meteorological station data (Yang et al., 2010) provided
144 meteorological inputs including precipitation, temperature and potential evapotranspiration.
145 Glacier coverages were extracted from the Second Glacier Inventory Dataset of China (Liu,
146 2012). The Tibetan Plateau Snow Cover Extent product (TPSCE, 5km×5km, Chen et al., 2018)
147 were used to denote the fluctuations of daily snow cover area (SCA) in the basins, which also
148 included the glacier cover area. The 8-day Leaf Area Index (LAI) and the monthly normalized
149 difference vegetation index (NDVI) data were downloaded from MODIS products of
150 MOD15A2H (500m×500m, Myneni et al., 2015) and MOD13A3 (1km×1km, Didan, 2015),
151 respectively. Soil parameters were estimated based on the soil properties extracted from the
152 1km × 1km Harmonized World Soil Database (HWSD, <http://www.fao.org/geonetwork>).

153 Daily streamflow during 2000-2010 for hydrological calibration were observed at the

154 Nuxia, Yangcun and Nugesha hydrological stations. Grab samples of precipitation and stream
 155 water were collected in 2005 at four stations along the main stream of YTR, i.e., Lazi (4889 m
 156 a.s.l.), Nugesha (4715 m a.s.l.), Yangcun (4541 m a.s.l.) and Nuxia (3691 m a.s.l.), from the
 157 upstream to the downstream (Fig. 1). Precipitation water were sampled as immediately as
 158 possible after the precipitation events, and stream water samples were collected weekly every
 159 Monday from the river. Considering the continental effect and elevation effect on precipitation
 160 isotope, the measured isotopic composition of precipitation from site sampling was interpolated
 161 by longitude and altitude (similar with [Zhao et al. 2012](#), [Liu et al. 2014](#)) using Eq. 1 to provide
 162 spatial precipitation isotope for model input, in which the coefficients x , y and z were estimated
 163 by least squares fitting the average precipitation $\delta^{18}\text{O}$ and corresponding altitude/longitude at
 164 the four measuring stations. The coefficient x reflected the altitudinal lapse of precipitation
 165 isotope, thus was expected to be lower than zero. Longitude reflected the distance from the
 166 station to the mainland border, thus the coefficient y was expected to be larger than 0. The term
 167 latitude was not chosen as a regression variable, because of the similar latitude of the
 168 measurement stations and the relatively narrow north-south range of the basin (Fig. 1). Isotopic
 169 composition of glacier meltwater was assumed to be constant during the entire study period,
 170 and lower than the amount weighted average isotopic composition of precipitation ([Boral and](#)
 171 [Sen, 2020](#)).

$$172 \quad \overline{\delta^{18}\text{O}_{precipitation}}(\text{‰}) = x * ALT(m) + y * LON(^{\circ}E) + z \quad (1)$$

173 Daily temperature and precipitation in the KR catchment during 2006-2012 were collected
 174 at the Langkazi meteorological Station. Altitudinal distributions of temperature and
 175 precipitation across the catchment were estimated by the lapse rates reported in [Zhang et al.](#)
 176 [\(2015\)](#). Daily streamflow during 2006-2012 for hydrological calibration and evaluation were
 177 measured at the Wengguo hydrological station. Grab samples of precipitation and stream water
 178 at the Wengguo Station in 2006-2007 and 2010-2012 were collected for isotope analysis.
 179 Isotopic composition of precipitation over elevation bands was calculated from the sampling
 180 site of Wengguo Station using an altitudinal lapse of $-0.34\text{‰}/100\text{m}$ reported in [Liu et al. \(2007\)](#).
 181 Isotopic composition of glacier meltwater in this catchment was assumed to be -18.9‰ ,
 182 constantly throughout the entire study period, adopting from the value reported in [Gao et al.](#)
 183 [2009](#)). Details of water samples in YTR and KR catchments are summarized in Table 1.

184 **[Table 1]**

185 **2.3 Isotopic General Circulation Model isoGSM and bias correction**

186 Precipitation $\delta^{18}\text{O}$ of the Scripps global spectral model with water isotopes-incorporated
 187 (isoGSM) developed by [Yoshimura et al. \(2008\)](#) was extracted to drive the tracer-aided model.
 188 IsoGSM was developed from the Scripps Experimental Climate Prediction Center's GSM,
 189 which was based on the medium range forecast model for making operational analysis and

190 predictions (Kanamitsu et al., 2002). Wang et al. (2017) evaluated the performance of ten iGCM
 191 datasets in five aspects of average isotope simulation, seasonal difference, temperature effect,
 192 precipitation effect and the global meteoric water line, ranking isoGSM as 1, 2, 1, 2 and 2
 193 respectively, indicating a relatively best performance of isoGSM among the iGCMs. The spatial
 194 and temporal resolutions of isoGSM dataset are $1.875^\circ \times 1.875^\circ$ and 6 hours, respectively.

195 The precipitation $\delta^{18}\text{O}$ estimated by isoGSM was corrected by site sampling measurements
 196 in Eqs. 2-4 before being used for hydrological model input. Biases between the amount
 197 weighted averages of isoGSM isotope and sampling measurement at the four sampling sites in
 198 YTR basin were calculated in Eq. 2 first. Spatial distribution of bias between isoGSM isotope
 199 and sampling measurement was then assumed as linearly related to altitude in Eq. 3, in which
 200 the coefficients of a and b were estimated by least squares fitting the site biases calculated in
 201 Eq. 2 and corresponding site altitudes. Daily isoGSM isotope data in hydrological model units
 202 over the study catchment were finally corrected in Eq. 4 using the unit altitudes.

$$203 \quad bias_i = \overline{\delta^{18}O_{i,m}} - \overline{\delta^{18}O_{i,G}} \quad i = 1,2,3,4 \quad (2)$$

$$204 \quad bias_r = a * ALT + b \quad (3)$$

$$205 \quad \begin{cases} bias_{r_k} = a * ALT_k + b \\ \delta^{18}O_{k,j,Corr} = \delta^{18}O_{k,j,G} + bias_{r_k} \end{cases} \quad (4)$$

206 where, $\overline{\delta^{18}O_{i,m}}$ is the amount weighted average of measured precipitation isotope over the
 207 sampling period in sampling site i ($i=1-4$), and $\overline{\delta^{18}O_{i,G}}$ is the amount weighted average of
 208 isoGSM precipitation isotope over the study period in pixel that contains the sampling site i .
 209 ALT is altitude of the sampling site or hydrological model unit. Parameters a and b are the linear
 210 regression coefficients. $\delta^{18}O_{k,j,Corr}$ and $\delta^{18}O_{k,j,G}$ are the corrected and original isoGSM
 211 precipitation isotope at all the hydrological model unit k ($k=1-63$) on the j^{th} day, respectively.
 212 Performance of the correction method of isoGSM data was evaluated by sampling measurement
 213 of precipitation isotope at the Wengguo station in the KR sub-basin, which was not involved in
 214 the estimation of coefficients a and b in Eq. 3. Spatial precipitation isotope of the isoGSM data
 215 in the KR sub-basin for hydrological modeling was estimated using the same altitudinal lapse
 216 that was used to interpolate the sampling data in Section 2.2, because the KR catchment only
 217 encompasses one pixel of the isoGSM data.

218 2.4 Tracer-aided hydrological model

219 A distributed tracer-aided hydrological model THREW-t (Tian et al., 2006; Nan et al., 2021)
 220 was adopted in this study for streamflow and isotope simulations. This model uses the
 221 Representative Elementary Watershed (REW) method for the spatial discretization of
 222 catchment, in which the study catchment is first divided into REWs based on the catchment
 223 DEM. Each REW is further divided into two vertical distributed layers (surface and subsurface

224 layers), including eight hydrological sub-zones according to land covers and soil properties
225 within the REW. Hydrological processes including canopy interception, infiltration,
226 infiltration-excess runoff, saturation-excess runoff and groundwater outflow were simulated in
227 each REW. REW is based on the self-similar characteristics of a watershed and its sub-
228 watersheds (Reggiani et al., 1999), and is regarded as the fundamental component of
229 hydrological processes and modelling, in which series of balance equations are established. The
230 principle of REW division is based on the scale of interest, modelling purpose, and the data
231 availability (Tian et al., 2006, 2008). In total, 63 and 41 REWs were extracted in YTR and KR,
232 respectively, which were adopted in two previous studies (Tian et al., 2020; Nan et al., 2021).
233 Areal averages of the gridded estimates of CMFD meteorological variables and precipitation
234 $\delta^{18}\text{O}$ were used in each of the REWs to drive the hydrological model. For application in cold
235 and high regions, a module representing the glacier melting and snowpack evolution was
236 incorporated into the original model in Tian et al. (2006), which has been proved as successful
237 in previous modelling works (e.g., He et al., 2015; Xu et al., 2019; Tian et al., 2020). The semi-
238 distributed REW-based structure made the model concise enough to couple the tracer module
239 easily. The tracer module was developed by Nan et al. (2021) which performed quite well on
240 reproducing the isotopic signature of stream water in the KR catchment. The isotope mixing
241 and fractionation processes were simulated based on the completely mixing assumption and the
242 Rayleigh fractionation method (Hindshaw et al., 2011; Wolfe et al., 2007). Forced by the input
243 data of precipitation isotope composition, the model can simulate the isotopic evolution all the
244 water bodies in the watershed, including soil water, snowpack, stream water, etc. The THREW-
245 t model considered the runoff components to stream water based on two aspects (Nan et al.,
246 2021). First is based on the individual water sources in the total water input forcing runoff
247 processes including rainfall, snowmelt and glacier melt. Second is based on the runoff-
248 generation processes including surface runoff and subsurface runoff (baseflow). The THREW-
249 t model mainly described the rainfall-runoff processes, thus only the role of shallow
250 groundwater which can be recharged by the rainfall was considered, but the contribution from
251 deep groundwater storage was not simulated. More details of model description and set up are
252 given in Tian et al. (2006) and Nan et al. (2021).

253 The physical basis and value ranges of the calibrated parameters in the THREW-t model
254 are described in Table 2. In both modeling catchments of YTR and KR, the parameter values
255 were optimized using three calibration variants: (1) a dual-objective calibration using observed
256 discharge and MODIS snow covered area fraction (SCA), (2) a triple-objective calibration
257 using observed discharge, MODIS SCA and $\delta^{18}\text{O}$ measurements of stream water forced by
258 linearly interpolated measurements of site sampling precipitation isotope, and (3) a triple-
259 objective calibration using observed discharge, MODIS SCA and $\delta^{18}\text{O}$ measurements of stream
260 water but forced by the isoGSM precipitation isotope data. Metrics used to evaluate the

261 simulations of discharge, SCA and isotope are list in Eqs. 5-7.

$$262 \quad NSE_{dis} = 1 - \frac{\sum_{i=1}^n (Q_{o,i} - Q_{s,i})^2}{\sum_{i=1}^n (Q_{o,i} - \overline{Q_o})^2} \quad (5)$$

$$263 \quad RMSE_{SCA} = \sqrt{\frac{\sum_{i=1}^n (SCA_{o,i} - SCA_{s,i})^2}{n}} \quad (6)$$

$$264 \quad MAE_{iso} = \frac{\sum_{i=1}^n |\delta^{18}O_{o,i} - \delta^{18}O_{s,i}|}{n} \quad (7)$$

265 where, n is the total number of observations. Subscripts of o and s refer to observed and
266 simulated variables, respectively. $\overline{Q_o}$ is the average value of observed streamflow during the
267 assessing period.

268 [Table 2]

269 An automatic procedure based on the pySOT optimization algorithm developed by
270 [Eriksson et al. \(2015\)](#) was implemented for all the three calibration variants to identify the
271 behavioral parameters. The pySOT used surrogate model to guide the search for improved
272 solutions, with the advantage of needing few function evaluations to find a good solution. An
273 event-driven framework POAP were used for building and combining asynchronous
274 optimization strategies. The optimization was stopped if a maximum number of allowed
275 function evaluations was reached, which was set as 3000 in this study. For both modeling
276 catchments, the pySOT algorithm was repeated 150 times for each calibration variant. Although
277 the measurement unit of NSE_{dis} is different from $RMSE_{SCA}$ and MAE_{iso} , their values are in the
278 same order of magnitude (0-1) when the model performances were acceptable ([Ala-aho et al.,](#)
279 [2017](#); [Nan et al., 2021](#)). Consequently, they were combined with equal weights for
280 simplification to represent the simultaneous performance on multiple objectives. For the dual-
281 and triple-objective calibration variants, $NSE_{dis} - RMSE_{SCA}$, $NSE_{dis} - RMSE_{SCA} - MAE_{iso}$ were
282 chosen as combined optimization objectives, respectively. Among the 150 final parameter sets
283 produced by the pySOT runs, the behavioral parameter sets were selected by NSE_{dis} thresholds,
284 i.e., only the parameter sets producing NSE_{dis} higher than an assumed threshold were regarded
285 as behavioral parameter sets. Considering the model behaviors in the two catchments, the NSE_{dis}
286 threshold was chosen as 0.85 for the YTR basin, and was chosen as 0.75 and 0.70 for dual- and
287 triple-objective calibration variants in KR catchment, respectively. Focusing on the utility of
288 isoGSM on forcing tracer-aided model, the influence of calibration objective function and
289 weight of each objective were not assessed in this study.

290 Considering the data availability, the calibration and validation periods for KR catchment
291 were set as 2006-2010 and 2011-2012, respectively. For YTR basin, discharge measured at the
292 outlet station Nuxia, the MODIS SCA fraction over the basin area upper the Nuxia station, and
293 the stream water $\delta^{18}O$ measured at the Nuxia station were used for calibration. Calibration and
294 validation periods of 2001-2005 and 2006-2010 were selected to test the model performance
295 for simulations of discharge and SCA at the Nuxia station. In addition, discharge measured at

296 the internal hydrological stations of Yangcun and Nugesha during 2001-2010 were used to
297 validate the spatial consistency of the calibrated model parameters. Model performance on
298 simulating stream water isotope at the Nuxia station in a validation period was not assessed as
299 stream water isotope measurements were available only during 2005. However, stream water
300 $\delta^{18}\text{O}$ measured during 2005 at the internal hydrological stations of Yangcun, Nugesha and Lazi
301 were adopted to validate the model performance on simulating spatial stream water $\delta^{18}\text{O}$ within
302 YTR basin.

303 **3. Results**

304 **3.1 Comparison between isoGSM and measured precipitation $\delta^{18}\text{O}$**

305 Figs. 2a and 3a show the comparison between isoGSM and measured precipitation $\delta^{18}\text{O}$ at
306 four sampling sites in the YTR basin. The isoGSM data presented similar fluctuations of
307 seasonal precipitation $\delta^{18}\text{O}$ to the sampling measurements (Fig. 3a). In particular, both isoGSM
308 and sampling measurement showed high precipitation $\delta^{18}\text{O}$ in May, and reached relatively low
309 values in the wet season during August and September. However, the original isoGSM data
310 tended to overestimate the measured precipitation $\delta^{18}\text{O}$ in the sampling periods (Fig. 2a). From
311 downstream to upstream, the amount weighted average precipitation $\delta^{18}\text{O}$ of samples collected
312 at the four stations (Nuxia, Yangcun, Nugesha and Lazi) were -9.58‰, -14.01‰, -14.80‰ and
313 -17.86‰, respectively, while the corresponding weighted average values of isoGSM pixels
314 containing the sampling stations during the same period were -7.53‰, -8.38‰, -9.22‰ and -
315 9.61‰, respectively. Bias between isoGSM data and sampling measurement tended to be larger
316 at upstream stations with higher elevations, partly due to the coarse spatial resolution of GCM
317 which cannot reproduce the effect of regional topography well. In contrast, the corrected
318 isoGSM data (black lines in Fig. 3a) captured the relatively low values in the late wet season
319 better than the original data (grey lines in Fig. 3a), and the scatter points fall closer to the 1:1
320 line (Fig. 2b). The MAE of isoGSM precipitation $\delta^{18}\text{O}$ in the YTR reduced from 6.65‰ to 4.91‰
321 after correction. Similarly, the original isoGSM data presented comparable seasonal
322 fluctuations of precipitation isotope to the sampling measurement at the Wengguo station in the
323 KR catchment (Fig. 3b), but the amount weighted average of precipitation $\delta^{18}\text{O}$ in the original
324 isoGSM data (-10.95‰) is much higher than that in the sampling measurement (-15.97‰, Fig.
325 2c and 3b). After bias correction, the overestimation was much reduced (Fig. 2d), indicated by
326 a reduced MAE value from 6.24‰ to 4.47‰. Underestimation of precipitation $\delta^{18}\text{O}$ by the
327 original isoGSM data in springs of 2011 and 2012, however, was not improved by the bias
328 correction.

329 **[Figure 2]**

330 **[Figure 3]**

331 Based on the multiple linear regression, the coefficients x , y and z in Eq. 1 were estimated
332 as -0.003, 0.574 and -52.6, respectively, with a R^2 value of 0.98, to interpolate the measured
333 isotope data to estimate spatial precipitation isotope over the YTR basin. The negative x and
334 positive y values were consistent with their physical meanings. Parameters a and b in Eq. 3
335 were estimated as -0.0046 and 14.96 based on the biases between isoGSM data and sampling
336 measurements on the four sampling sites in YTR. Fig. 4 and Fig.5 show the comparison of the
337 amount weighted averages of precipitation $\delta^{18}\text{O}$ on 63 REWs derived from the corrected
338 isoGSM data and interpolated sampling measurement. It is shown that the distributions of
339 precipitation isotope with altitude were rather similar in the two datasets (Fig. 4b). However,
340 distributions across the longitudes show visible differences. The largest differences between the
341 two datasets were located in the west upstream region (longitude $< 86^\circ$) and the source region
342 of tributary Lhasa River ($93^\circ > \text{longitude} > 86^\circ$, latitude $> 30^\circ$) (Fig. 4a and 5). In comparison
343 to the corrected isoGSM data, the interpolated sampling measurement estimated much lower
344 isotope signature in the upstream region, while presenting higher isotope signature in the upper
345 Lhasa River. As site sampling data of precipitation was insufficient to test which of the two
346 datasets captured the west-east distribution of precipitation isotope better, model performance
347 on simulating isotope signatures of stream water measured at hydrological stations from west
348 to east forced by the two datasets provide a perspective to assess the precipitation isotope
349 estimations.

350 [Figure 4]

351 [Figure 5]

352 3.2 Model performance for the simulations of discharge and stream water isotope

353 Fig. 6-7 and Table 3 show the model performance of different calibration variants in the
354 YTR basin produced by the behavioral parameter sets. The three calibration variants produced
355 similar simulations of discharge and SCA (Fig. 6), in spite of the slightly higher NSE_{dis} and
356 lower RMSE_{SCA} estimated by the dual-objective calibration (Table 3). For the simulation of
357 stream water $\delta^{18}\text{O}$, the dual-objective calibration produced the worst MAE_{iso} values in three out
358 of the four testing stations with the largest uncertainty ranges (Fig. 7a), which can be expected
359 as isotope data was not involved in this calibration. The two triple-objective calibration variants
360 produced good simulation for the stream water isotope at the Nuxia station in the calibration
361 year of 2005 (Fig. 7b and 7c). However, the triple-objective calibration variant forced by
362 isoGSM data estimated worse performance (i.e., higher MAE_{iso} values) for stream water $\delta^{18}\text{O}$
363 at the stations of Yangcun and Nugesha than the calibration forced by interpolated sampling
364 measurement showing significant underestimations for peak isotope values in June at Yangcun
365 station, and higher overestimations for isotope values after August at Nugesha. This was due to
366 the poor performance of isoGSM on capturing the isotope signature of individual precipitation

367 events during a specific period (see Fig. 3a), although being corrected already. For example,
368 the amount weighted average of measured precipitation $\delta^{18}\text{O}$ in June at the Yangcun station was
369 -5.87‰ , while the average of corrected isoGSM data showed a value of -10.09‰ , leading to
370 an underestimated peak value. Similarly, the amount weighted average of measured
371 precipitation $\delta^{18}\text{O}$ at Nugesha during August was -16.34‰ , while the corrected isoGSM data
372 estimated an average of -11.47‰ , leading to an overestimated stream $\delta^{18}\text{O}$ in the late wet season.
373 In spite of that, the performance of simulated stream water $\delta^{18}\text{O}$ at Nuxia, Yangcun and Nugesha
374 stations forced by corrected isoGSM data can still be considered as acceptable, given the
375 MAE_{iso} values were generally around 1 (Fig. 7c). For the most upstream station Lazi, however,
376 the triple-objective variant forced by measured precipitation $\delta^{18}\text{O}$ produced significantly
377 underestimated $\delta^{18}\text{O}$ of stream water, likely due to the underestimated precipitation $\delta^{18}\text{O}$ in the
378 upstream high altitudes produced by the interpolated measurement data (Fig. 4a and 5). The
379 good performance of simulated stream water $\delta^{18}\text{O}$ at the Lazi station driven by the corrected
380 isoGSM data demonstrated that the corrected isoGSM estimated a better precipitation isoscape
381 in high altitudes of the study catchment than the linearly interpolated measurement data, partly
382 benefiting from the information of spatial precipitation isotope implied in the gridded values.
383 It is worth noting that the model simulations forced by corrected isoGSM estimated narrower
384 uncertainty bands for stream water $\delta^{18}\text{O}$ at Nuxia, Yangcun and Nugesha, and smaller value
385 ranges of the MAE_{iso} metric at all the four stations, in comparison to the simulations driven by
386 the interpolated precipitation $\delta^{18}\text{O}$. Compared to the simulations yielded by the dual-objective
387 calibration, the triple-objective calibration variants simulated smaller uncertainty ranges for
388 stream water $\delta^{18}\text{O}$ and slightly narrowed value ranges of objective metrics for the simulations
389 of discharge and SCA with the lower behavioral ratios of calibrated parameter sets in Table 3,
390 indicating good potential of isotope data on reducing modeling uncertainty and improving
391 parameter identifiability.

392 **[Figure 6]**

393 **[Figure 7]**

394 **[Table 3]**

395 The simulated hydrographs at two internal hydrological stations of Yangcun and Nugesha
396 were compared in Fig. 8 to assess the spatial consistency of model parameters calibrated by the
397 different variants. The isoGSM-forced triple-objective calibration produced the highest
398 performance for discharge simulation at the two internal stations (Fig. 8e and 8f) indicated by
399 the highest averages (0.82 and 0.74 for Yangcun and Nugesha) and minimal values (0.72 and
400 0.53 for Yangcun and Nugesha) of NSE, as well as the smallest values ranges of NSE. The dual-
401 objective calibration produced lower performance for discharge simulation than the isoGSM-
402 forced triple-objective calibration (with average NSE as 0.8 and 0.67 at Yangcun and Nugesha)
403 with a much larger uncertainty of the baseflow simulation (Fig. 8a and Fig. 8b). The

404 interpolation-forced triple-objective calibration produced higher mean NSE (0.81 and 0.74 for
405 Yangcun and Nugesha) but smaller minimal NSE (0.62 and 0.31 for Yangcun and Nugesha)
406 than the dual-objective calibration with the largest values ranges of NSE at the two stations.
407 Moreover, the isoGSM-forced triple-objective calibration performed best on capturing the peak
408 flows in summer at both stations.

409 **[Figure 8]**

410 The model performances produced by the behavioral parameter sets of different calibration
411 variants in the KR catchment were shown in Figs. 9-10 and Table 4. All the three calibration
412 variants presented similar performances on simulating streamflow, while the two triple-
413 objective calibrations resulted in narrower uncertainty ranges, especially for the baseflow (Fig.
414 9c and e). The declining SCA in spring-summer was captured well in all the calibration variants
415 (Figs. 9b, d and f). Triple-objective calibrations driven by the two isotope datasets performed
416 comparably well on simulating the isotopic composition of stream water in the calibration
417 period (Fig. 10b and 10c) indicated by the low average values of MAE_{iso} (0.68 and 0.69) and
418 the well captured seasonal fluctuations of stream water $\delta^{18}O$. The peak isotopic values in around
419 June of 2007 were not captured well by the isoGSM-driven model (Fig. 10c), resulting in a
420 relatively larger minimal MAE_{iso} (0.57) than the interpolated measurement-driven result (0.48).
421 This was due to the underestimations of isoGSM on estimating the isotope signatures of
422 individual extreme precipitation events in June (see Fig. 3b). Specifically, there was a
423 precipitation event larger than 20mm/day in June of 2007, of which the corrected isoGSM
424 produced significantly lower $\delta^{18}O$ (-21.55‰) than the sampling measurement (-9.83‰) at the
425 Wengguo station. Despite that, the isoGSM-forced triple-objective calibration estimated much
426 better performance than the interpolated measurement-driven calibration for stream water $\delta^{18}O$
427 in the validation period (Figs. 10b and c). Similar to YTR, the triple-objective calibrations got
428 much smaller behavioral parameter sets (19 and 18 for measurement- and isoGSM-forced
429 calibration variants) than the dual-objective calibration (117) through 150 runs of the automatic
430 calibration program, indicating strongly increased identifiability of model parameters and
431 reduced uncertainty by the using of isotope data.

432 **[Figure 9]**

433 **[Figure 10]**

434 **[Table 4]**

435 **3.3 Contributions of runoff components**

436 Fig. 11 and Tables 5-6 compare the proportions of water sources in the annual water input
437 for runoff generation simulated by the behavioral parameter sets identified by the three
438 calibration variants. In the KR sub-basin (Fig. 11b and Table 6), rainfall provided the largest
439 volume of water source for runoff generation simulated by the three calibration variants

440 (44.2%-47.4%), followed by glacier meltwater (29.2%-33.8%). Snowmelt contributed the
441 lowest proportion of 22.0%-23.4% in the total water input. The two triple-objective calibrations
442 estimated very similar contributions of runoff component, and consistently estimated lower
443 proportions of glacier melt than the dual-objective calibration, which can be attributed to the
444 role of isotope data in regulating the contribution of strong-evaporated surface runoff
445 component fed by glacier melt to streamflow (Nan et al., 2021) by rejecting parameter sets that
446 estimated small proportions of rainfall but large proportions of glacier melt (as shown by the
447 error bar in Fig. 11b). Meanwhile, uncertainties of the estimated contributions were
448 significantly reduced (from 9.4% to 6.2% and 4.7%, Table 6) by integrating isotope data into
449 the model. Regarding the contributions of water sources to seasonal water input, snowmelt and
450 rainfall were the dominant water sources in spring and summer. Three water sources had similar
451 contributions during autumn. Glacier melt produced a relatively steady contribution of around
452 30%-35% throughout the year. Similar to the annual contributions, seasonal contributions of
453 snowmelt and rainfall estimated by the two triple-objective calibrations were larger than those
454 estimated by the dual-objective calibration, while the opposite holds true for the seasonal
455 contributions of glacier melt. The largest differences of the contributions estimated by the
456 different calibration variants go to the winter season (Table 6), which however had negligible
457 effect on the annual runoff regime because of the extremely low contribution of water input in
458 this season (<1%). Uncertainties of the runoff component contributions were reduced by
459 involving isotope calibration most significantly during summer, because the isotope data
460 brought more constraint on the rainfall-runoff processes, which played dominant role in summer.
461 The uncertainties of annual contributions were close to those of summer contributions because
462 of the large proportion of water input to annual runoff in summer (>60%). In contrast,
463 uncertainties of winter contributions estimated by the triple-objective calibration variants
464 tended to be larger than that estimated by the dual-objective calibration, due to the smaller
465 amount of total water input in winter as a result of lower contribution of meltwater estimated
466 by triple-objective variants.

467 In the YTR catchment, rainfall showed larger dominance on annual runoff than glacier and
468 snow meltwater with the mean contributions of 61.4%-69.6% (Fig. 11a and Table 5). The dual-
469 objective calibration and triple-objective calibration forced by measured isotope data estimated
470 similar annual contributions of rainfall (~62%), snowmelt (~11%) and glacier melt (~27%).
471 Nonetheless, the isoGSM-forced triple-objective calibration estimated significantly higher
472 mean proportion of rainfall (70%) but lower mean proportion of glacier melt (18%) by rejecting
473 the parameter sets that estimated rainfall contributions less than 60% and glacier melt
474 contributions more than 30%, which however were identified to be acceptable in the other two
475 calibration variants (as shown by the error bar in Fig. 11a). Difference of the glacier melt
476 contributions estimated by the two triple-objective calibration variants mainly resulted from the

477 difference of precipitation $\delta^{18}\text{O}$ inputs from the two datasets. The interpolated measurement
478 data tended to produce higher precipitation $\delta^{18}\text{O}$ in the middle and downstream regions of YTR
479 basin but lower values in the upstream region, compared to the corrected isoGSM data (Fig.
480 4b). Meanwhile, the precipitation input in the downstream region was higher than that occurred
481 in the upstream (Xu et al., 2017), thus resulting in higher average precipitation $\delta^{18}\text{O}$ over the
482 entire YTR of the interpolated measurement data. Consequently, larger contribution of glacier
483 melt with low isotope composition was estimated in the interpolated interpolation-forced triple-
484 objective calibration to counteract the effect of precipitation input with high isotopic
485 composition for matching the measured stream water $\delta^{18}\text{O}$. By involving isotope simulation,
486 both triple-objective variants significantly reduced the uncertainties of the estimated
487 contributions (from 11.9% to 8.6% and 8.9%, Table 5). Similar to the estimated annual
488 contributions, the isoGSM-forced triple-objective calibration estimated higher mean proportion
489 of rainfall, lower mean proportion of glacier melt and comparable mean proportion of snowmelt
490 in the four seasons, compared to the dual-objective calibration and triple-objective calibration
491 forced by measured isotope data. In general, rainfall was the dominant water input source in
492 summer and autumn, and snowmelt dominated the runoff in winter. The contributions of rainfall
493 and snowmelt to total water input were close in spring. Similar to KR catchment, uncertainty
494 of runoff component contribution was reduced by the isotope-involved calibrations more
495 significantly in seasons when rainfall played dominant roles.

496 [Figure 11]

497 [Table 5]

498 [Table 6]

499 4. Discussion

500 4.1 Uncertainties and limitations of the tracer-aided hydrological model

501 Integrating the simulations of water isotope signatures into the hydrological model
502 structure could help to make use of hydrological information additionally implied in the water
503 isotope data without introducing new model parameters for the runoff processes. However,
504 uncertainty of the simulation of water isotope in the tracer-aided hydrological model can be
505 caused by the following sources. First, the isotopic compositions of meltwater sources were
506 determined based on simplified assumptions, which however were hard to verify in a large
507 basin due to the limited field sampling work. The isotopic compositions of glacier melt were
508 assumed as constant throughout the modeling period due to the unavailability of glacier melting
509 water samples. Large number of studies reported that the isotope composition of glacier melt
510 had very small variability, and the value were much lower than that of precipitation (e.g., Boral
511 & Sen, 2020; Cable et al., 2011; He et al., 2019; Rai et al., 2019; Wang et al., 2016). Considering

512 that the changes of glacier elevation during the 10-year modeling period were small, indicating
513 that ice melt on the glacier surface in each of the summer seasons occurred very likely from the
514 same elevation bands with similar isotopic compositions, the assumption on glacier melt
515 isotope adopted in this study was reasonable. However, the assumed isotope composition of
516 glacier melt will no doubt influence the modelling result, especially the estimated contribution
517 of water sources. Specifically, a lower assumed value of glacier melt isotope composition led
518 to a lower contribution of isotopic depleted glacier melt runoff component. As for the snow
519 meltwater, the isotopic evolution was simulated according to the mass balance of snowpack
520 similarly with other water storages. The isotope fractionation effect caused by the melt
521 processes was inadequately characterized in our model, which could lead to uncertainty in the
522 simulation of snowmelt isotope (Pu et al., 2020).

523 Second, the uncertainty of the precipitation isotope input data served as another uncertainty
524 source of the isotope simulation in the model. Although the isotope data itself had no influences
525 on the hydrological processes, the calibration procedure to fit the simulated stream isotope
526 signature with observation indeed affected the model simulations of runoff processes (Delavau
527 et al., 2017). For the sampling measurement-based forcing data, the uncertainty came from the
528 interpolation procedure. We used a linear interpolation method based on longitude and altitude
529 to estimate the precipitation isoscape. This could be reasonable in our study catchment because
530 these two factors characterize the major spatial pattern and altitude effect of precipitation
531 isotope in similar large-scale regions on TP (Liu et al., 2014). However, low availability of site
532 measurement data derived from the sparse water sampling network led to large uncertainty
533 of the interpolated result. All the four sampling stations were located at around the same latitude,
534 and cannot reflect latitude effect on precipitation isotope (Dansgaard, 1964). Measurements
535 from more water sampling sites are required in the future for the improvement of the
536 interpolation method. For the isoGSM data, uncertainty came from its coarse spatial resolution.
537 Although the isoGSM data bears the potential to capture spatial patterns of precipitation isotope
538 in large basins, the effect of regional topography on isotope was not reflected well in the current
539 product due to its rather coarse pixel size (~200km×200km). Consequently, developing
540 downscale methods that are applicable to mountainous catchments to extract regional isotope
541 estimates from iGCM products (such as iRCM in Sturm et al., 2007) might be helpful for the
542 tracer-aided hydrological modelling on the TP. Moreover, the bias-correction procedure based
543 on measurements from a sparse water sampling network inevitably brought uncertainty to the
544 corrected isoGSM data. The current sampling sites of precipitation are located along the river
545 channel with elevations lower than the contributing mountains, thus failing to involve isoGSM
546 estimates at high mountainous terrains into the correction procedure. The terms used in Eq. 3
547 (only elevation) to correct isoGSM were different from that in Eq. 1 (elevation and longitude)
548 to interpolate the measurement data. The error of isoGSM tended to be larger in higher elevation

549 regions, because of the complex regional topography which cannot be captured well by the
550 coarse spatial resolution of isoGSM, but there was no mechanism making the error of isoGSM
551 change with longitude. Consequently, the term longitude was deprecated in Eq. 3 rather than
552 the interpolation equation. However, the choice of regression terms in interpolation and bias
553 correction undoubtedly had significant influence on the modelling result, which could be
554 another important source of uncertainty.

555 The modelling uncertainty is highly related to the model structure and parameters, and our
556 results indicated that the additional information from isotope data reduced uncertainty of
557 parameters. However, global climate changes are changing streamflow regimes on the TP (e.g.,
558 [Xu et al., 2019](#); [Lin et al., 2020](#); [Yong et al., 2021](#)), which may request a changing model
559 structure as well. In this study, the model structure was not modified, thus the changing
560 conditions were far less than adequately represented in the current model, due to lack of
561 adequate understanding of the influence of changing condition on runoff generation mechanism.
562 However, some of the changing underlying conditions can also be reflected by the parameters.
563 For example, frozen ground degradation can lead to a larger water storage capacity and higher
564 hydraulic conductivity, which can be reflected by the parameters WM, KKA and KKD in our
565 model. Meanwhile, the tracer-aided hydrological modelling method can also help diagnose the
566 model structure (e.g., [Birkel et al., 2011](#)), but such work has been only conducted in small
567 catchments due to the limited precipitation isotope input data in large scale. This study mainly
568 explored the utility of iGCM data on forcing tracer-aided model in large basins, thus provided
569 the potential to conduct the works improving model structure in large basin scale. For the
570 simulation in YTR basin in this study, the model was applied at a relatively short time scale
571 (less than one decade), during which the change condition was not an important issue. To
572 expand the result to a longer time scale and to predict the future streamflow trend, more work
573 is needed to consider the variation of model structures and parameters.

574 **4.2 The value of spatial precipitation isotope data derived from iGCM for aiding** 575 **hydrological modeling in large basins**

576 Comparisons with the dual-objective calibration without isotope data indicated high value
577 of spatial precipitation isotope data for reducing modeling uncertainty. To better understand the
578 role of isotope data, we analyzed the relationship between the behaviors of discharge and
579 isotope simulations obtained by the calibration without isotope (dual-objective calibration).
580 There was a trade-off between the two objectives (Fig. 12a). The highest NSE_{dis} can reach
581 around 0.93, but the MAE_{iso} was not good at the same time. When MAE_{iso} reach relative best
582 values, the NSE_{dis} was around 0.9, which exhibited a high-level performance as well. The
583 relationship between model performance and estimated glacier melt contribution was further
584 explored, and it was found that when the highest NSE_{dis} was obtained, the contribution of

585 glacier melt was estimated as around 0.35~0.4, which was however estimated as around 0.2
586 when best MAE_{iso} was obtained (Fig. 12b and c). The isotope composition of glacier melt was
587 assumed to be lower than the precipitation, thus an overestimated contribution of glacier melt
588 can lead to lower simulated river isotope than measurement. Consequently, calibration focusing
589 only on discharge may result in overestimated glacier melt, which can be rejected by the
590 behavior of isotope simulation. It is notable that the performance of isotope simulation is more
591 sensitive than discharge simulation to the runoff component and internal processes. When the
592 contribution of glacier melt is in a large range of 10-40%, the NSE_{dis} can all be calibrated to a
593 high value (>0.9) by adjusting other parameters, whereas the MAE_{iso} gets worse significantly
594 when the proper contribution of water source is deviated.

595 **[Figure 12]**

596 Model simulations forced by the two precipitation isotope datasets produced similar total
597 streamflow simulation in the YTR basin, but resulted in certain difference in the simulated
598 stream water isotopic composition and water source apportionments, which was consistent with
599 the findings in [Delavau et al. \(2017\)](#). The choice of precipitation isotope input data was
600 demonstrated to have large influence on the model performance. In this study, model
601 simulations forced by the corrected isoGSM data performed better than that driven by the
602 interpolated data of sampling measurement with respect to discharge and stream water isotope
603 simulations at internal hydrological stations. The fact that model can simultaneously satisfy
604 multiple calibration objectives gave confidence in the model realization and robustness
605 ([McDonnell and Beven, 2014](#)), consequently resulting in the consistent model behavioral
606 performances in both outlet and internal stations.

607 Beyond the model performance on discharge and isotope simulation, three aspects of
608 evidences indicated the results of model forced by isoGSM data to be more likely reasonable.
609 Firstly, the runoff component contributions estimated by the isoGSM-forced triple-objective
610 calibration were likely more reliable than those estimated by the dual-objective and the
611 interpolation-forced triple-objective calibrations. Contribution of glacier melt to annual water
612 input in the YTR basin was estimated as around 27% in the dual-objective and the interpolation-
613 forced triple-objective calibrations, which was more unlike to be true considering the small
614 glacier covered area ratio (2%). Glacier melt contribution estimated by the isoGSM-forced
615 triple-objective calibration was lower than 20%, within the ranges reported by some previous
616 studies ([Immerzeel et al., 2010](#); [Bookhagen and Burbank, 2010](#); [Zhang et al., 2013](#)). Secondly,
617 the average calibrated melting threshold temperature (T_0) and glacier degree-day factor (DDF_G)
618 of YTR basin obtained by the isoGSM-forced triple-objective calibration were 0.75°C and
619 7.43mm/d/°C. This was consistent with the reported results estimated in a manner by glacier
620 mass balance measurements, that the YTR basin was in the region with DDF_G ranging from 6-
621 9 mm/d/°C estimated by the T_0 of 0°C ([Zhang et al., 2006](#)). On the contrary, although the

622 calibrated DDF_G obtained by dual-objective and interpolation-forced triple-objective
623 calibration were still within the range of 6-9 (7.98 and 8.37 mm/ d/°C, respectively), the T_0
624 values were calibrated as -1.41 and -1.49°C, respectively, much lower than the value adopted
625 in [Zhang et al. \(2006\)](#), resulting in overestimated glacier melt runoff. Thirdly, the THREW-t
626 model also quantified the runoff component in terms of runoff generation pathway, and divided
627 the runoff into surface runoff and baseflow. The contribution of baseflow was estimated as
628 29.26 km³/yr by the isoGSM-forced triple-objective calibration, which was very close to the
629 result (30km³/yr) estimated by the groundwater model MODFLOW-NWT independently from
630 hydrological modeling approach reported in [Yao et al. \(2021\)](#), whereas the baseflow estimated
631 by dual-objective and interpolation-forced triple-objective were much lower (24.04 and 22.47
632 km³/yr, respectively). A more reliable baseflow estimation likely helped improve the
633 reasonability of modelling result, and reduce equifinality by constraining the parameters related
634 to groundwater.

635 Above results indicated that the corrected isoGSM product served as a better choice to
636 force the tracer-aided hydrological model than the interpolated data of sampling measurement.
637 It is commonly difficult to estimate the precipitation isoscapes in large mountainous catchments
638 according to limited available site sampling data. Relatively, the iGCM data has the advantage
639 of presenting more spatial information of precipitation isotope via physically simulating the
640 processes of vapor transfer, condensation and supersaturation in the atmosphere and their
641 effects on precipitation isotope ([Xi, 2014](#)). Our results indicated that even precipitation isotope
642 measurements at only four sampling sites provided sounds good ground data basis to correct
643 the isoGSM isotope product in the study basin with a size of 2×10^5 km². The condition was
644 different in the KR sub-catchment, where the triple-objective variants forced by two isotope
645 datasets performed similarly with respect to discharge and isotope simulation and runoff
646 component contribution estimation. This is due to the much smaller catchment area than the
647 pixel size, thus the advantage of the spatial information provided by isoGSM was not taken
648 adequately. To develop a general strategy for establishing tracer-aided in large basin, especially
649 in the regions where limited measured precipitation isotope data is available, as less information
650 from measurement data as possible was used to correct the isoGSM data. Consequently, only
651 the average value of measured isotope data was used to correct the isoGSM (Eq. 2), and the
652 seasonal characteristic of the bias was not considered (such as in [Delavau et al., 2017](#)). Our
653 results indicated that even being corrected by only four average values, isoGSM can perform
654 well on capturing seasonal fluctuation of precipitation isotope and forcing tracer-aided model
655 in YTR basin, thus bears the potential to serve as input isotope data in data sparse regions. The
656 influence of iGCM/iRCM product and bias correction method was not discussed in detail in
657 this study, which is however an important issue and need further exploration.

658 **5. Conclusions**

659 The utility of precipitation isotope input derived from the Isotopic General Circulation
660 Models (iGCM) product isoGSM in forcing the distributed tracer-aided hydrological model
661 THREW-t in a large basin of $2 \times 10^5 \text{ km}^2$ on the Tibetan Plateau (TP) was investigated in this
662 study. Model performance driven by the isoGSM data was evaluated by comparing with
663 simulations driven by precipitation isotope measurements from a sparse sampling network. Our
664 main findings are:

665 (1) Spatial precipitation isotope data derived from the Isotopic General Circulation Models
666 helped to reduce modeling uncertainty and improve parameter identifiability, in comparison to
667 a calibration method using discharge and snow cover area fraction without any information of
668 water isotope. The developed tracer-aided hydrological model forced by the isoGSM data
669 showed high values for robustly representing runoff processes in large mountainous catchments.

670 (2) Model parameters estimated by the isoGSM data corrected using site sampling
671 measurements of precipitation isotope presented higher transferability to nested sub-basins and
672 produced higher model performance in the validation period than that estimated by the
673 interpolated isotope data from site sampling measurement. The smaller uncertainty ranges of
674 model simulations in nested sub-basins forced by the corrected isoGSM data further indicated
675 that the corrected isoGSM data served as a better choice to provide informative spatial
676 precipitation isotope in large basins than the interpolated data from site sampling measurements.

677 (3) Using the corrected isoGSM data improved the quantification of contributions of runoff
678 components to streamflow on both annual and seasonal scales. Model calibration procedure
679 forced by the corrected isoGSM data successfully rejected parameter sets that estimated
680 overestimation of glacier melt contribution, indicating that precipitation isotope measurements
681 at only four sampling sites along the river channel provided a good ground data basis to correct
682 the isoGSM product in the study catchment.

683 **Code/Data availability**

684 The isotope data and the code of THREW-t model used in this study are available by contacting
685 the authors.

686 **Author contribution**

687 YN, ZH and FT conceived the idea; ZW provided the isoGSM data; LT provided the
688 measurement isotope data; YN, ZH and FT conducted analysis; ZW and LT provided comments
689 on the analysis; all the authors contributed to writing and revisions.

690 **Competing interests**

691 The authors declare that they have no conflict of interest.

692 **Acknowledgements**

693 This study was supported by the National Key R&D Program of China (2018YFC1508103)
694 and the National Science Foundation of China (92047301). The authors thank all the
695 organizations and scientists for the contribution of data used in this work. All the data used in
696 this study will be available on request from the corresponding author (tianfq@tsinghua.edu.cn).

697 **Financial support**

698 This study was supported by the National Key R&D Program of China (2018YFC1508103)
699 and the National Science Foundation of China (92047301).

700

701 **References**

- 702 Ala-aho, P., Tetzlaff, D., McNamara, J. P., Laudon, H., & Soulsby, C. (2017). Using isotopes to
703 constrain water flux and age estimates in snow-influenced catchments using the STARR
704 (Spatially distributed Tracer-Aided Rainfall–Runoff) model. *Hydrology and Earth System
705 Sciences*, 21(10), 5089-5110. doi:10.5194/hess-21-5089-2017
- 706 Birkel, C., & Soulsby, C. (2015). Advancing tracer-aided rainfall-runoff modelling: a review of
707 progress, problems and unrealised potential. *Hydrological Processes*, 29(25), 5227-5240.
708 doi:10.1002/hyp.10594
- 709 Birkel, C., Tetzlaff, D., Dunn, S. M., & Soulsby, C. (2011). Using time domain and geographic
710 source tracers to conceptualize streamflow generation processes in lumped rainfall-runoff
711 models. *Water Resources Research*, 47(2). doi:10.1029/2010wr009547
- 712 Bookhagen, B., & Burbank, D. W. (2010). Toward a complete Himalayan hydrological budget:
713 Spatiotemporal distribution of snowmelt and rainfall and their impact on river discharge.
714 *Journal of Geophysical Research*, 115(F3). doi:10.1029/2009jf001426
- 715 Boral, S., & Sen, I. S. (2020). Tracing ‘Third Pole’ ice meltwater contribution to the Himalayan
716 rivers using oxygen and hydrogen isotopes. *Geochem. Perspect. Lett*, 13, 48-53.
- 717 Cable, J., Ogle, K., & Williams, D. (2011). Contribution of glacier meltwater to streamflow in
718 the Wind River Range, Wyoming, inferred via a Bayesian mixing model applied to isotopic
719 measurements. *Hydrological Processes*, 25(14), 2228-2236.
- 720 Capell, R., Tetzlaff, D., & Soulsby, C. (2012). Can time domain and source area tracers reduce
721 uncertainty in rainfall-runoff models in larger heterogeneous catchments? *Water
722 Resources Research*, 48(9). doi:10.1029/2011wr011543
- 723 Chen, X., Long, D., Liang, S., He, L., Zeng, C., Hao, X., & Hong, Y. (2018). Developing a
724 composite daily snow cover extent record over the Tibetan Plateau from 1981 to 2016
725 using multisource data. *Remote Sensing of Environment*, 215, 284-299.
726 doi:10.1016/j.rse.2018.06.021
- 727 Dansgaard, W.: Stable isotopes in precipitation, *Tellus*, 16, 436–468, 1964.
- 728 Delavau, C. J., Stadnyk, T., & Holmes, T. (2017). Examining the impacts of precipitation
729 isotope input ($\delta^{18}\text{O}$) on distributed, tracer-aided hydrological modelling. *Hydrology and
730 Earth System Sciences*, 21(5), 2595-2614. doi:10.5194/hess-21-2595-2017

731 Didan, K. (2015). MOD13A3 MODIS/Terra vegetation Indices Monthly L3 Global 1km SIN
732 Grid V006 [Data set]. NASA EOSDIS Land Processes DAAC. Accessed 2020-01-01 from
733 <https://doi.org/10.5067/MODIS/MOD13A3.006>

734 Dong, W., Lin, Y., Wright, J. S., Ming, Y., Xie, Y., Wang, B., . . . Xu, F. (2016). Summer rainfall
735 over the southwestern Tibetan Plateau controlled by deep convection over the Indian
736 subcontinent. *Nature Communications*, 7. doi:10.1038/ncomms10925

737 Duethmann, D., Bolch, T., Farinotti, D., Kriegel, D., Vorogushyn, S., Merz, B., . . . Güntner, A.
738 (2015). Attribution of streamflow trends in snow and glacier melt-dominated catchments
739 of the Tarim River, Central Asia. *Water Resources Research*, 51(6), 4727-4750.
740 doi:10.1002/2014wr016716

741 Eriksson, D., Bindel, D., & Shoemaker, C. (2015). Surrogate optimization toolbox (pysot).

742 Gao, J., Tian, L. D., & Liu, Y. Q. (2009). Oxygen isotope variation in the water cycle of the
743 Yamdrok-tso Lake Basin in southern betan Plateau. *Chinese Science Bulletin*, 54(15),
744 2153-2159.

745 Gupta, H. V., Wagener, T., & Liu, Y. (2008). Reconciling theory with observations: elements of
746 a diagnostic approach to model evaluation. *Hydrological Processes*, 22(18), 3802-3813.
747 doi:10.1002/hyp.6989

748 He, Z., Unger-Shayesteh, K., Vorogushyn, S., Weise, S. M., Kalashnikova, O., Gafurov, A., . . .
749 Merz, B. (2019). Constraining hydrological model parameters using water isotopic
750 compositions in a glacierized basin, Central Asia. *Journal of Hydrology*, 571, 332-348.
751 doi:10.1016/j.jhydrol.2019.01.048

752 He, Z., Vorogushyn, S., Unger-Shayesteh, K., Gafurov, A., Kalashnikova, O., Omorova, E., &
753 Merz, B. (2018). The Value of Hydrograph Partitioning Curves for Calibrating
754 Hydrological Models in Glacierized Basins. *Water Resources Research*, 54(3), 2336-2361.
755 doi:10.1002/2017wr021966

756 He, Z. H., Tian, F. Q., Gupta, H. V., Hu, H. C., & Hu, H. P. (2015). Diagnostic calibration of a
757 hydrological model in a mountain area by hydrograph partitioning. *Hydrology and Earth
758 System Sciences*, 19(4), 1807-1826. doi:10.5194/hess-19-1807-2015

759 He, Z., Yang, L., Tian, F., Ni, G., Hou, A., & Lu, H. (2017). Intercomparisons of Rainfall
760 Estimates from TRMM and GPM Multisatellite Products over the Upper Mekong River
761 Basin. *Journal of Hydrometeorology*, 18(2), 413-430. doi:10.1175/jhm-d-16-0198.1

- 762 Hindshaw, R. S., Tipper, E. T., Reynolds, B. C., Lemarchand, E., Wiederhold, J. G., Magnusson,
763 J., . . . Bourdon, B. (2011). Hydrological control of stream water chemistry in a glacial
764 catchment (Damma Glacier, Switzerland). *Chemical Geology*, 285(1-4), 215-230.
765 doi:10.1016/j.chemgeo.2011.04.012
- 766 Immerzeel, W. W., Pellicciotti, F., & Bierkens, M. F. P. (2013). Rising river flows throughout
767 the twenty-first century in two Himalayan glacierized watersheds. *Nature Geoscience*, 6(9),
768 742-745. doi:10.1038/ngeo1896
- 769 Immerzeel, W. W., van Beek, L. P. H., & Bierkens, M. F. P. (2010). Climate Change Will Affect
770 the Asian Water Towers. *Science*, 328(5984), 1382-1385. doi:10.1126/science.1183188
- 771 Kanamitsu, M., Kumar, A., Juang, H. M. H., Schemm, J. K., Wang, W. Q., Yang, F. L., . . . Ji,
772 M. (2002). NCEP dynamical seasonal forecast system 2000. *Bulletin of the American*
773 *Meteorological Society*, 83(7), 1019-+. doi:10.1175/1520-
774 0477(2002)083<1019:Ndsfs>2.3.Co;2
- 775 Li Z., Qi, F., Zongjie, L., Ruifeng, Y., Juan, G., & Yuemin, L. (2019). Climate background, fact
776 and hydrological effect of multiphase water transformation in cold regions of the Western
777 China: A review. *Earth-Science Reviews*, 190, 33-57. doi:10.1016/j.earscirev.2018.12.004
- 778 Lin, L., Gao, M., Liu, J., Wang, J., Wang, S., Chen, X., & Liu, H. (2020). Understanding the
779 effects of climate warming on streamflow and active groundwater storage in an alpine
780 catchment: the upper Lhasa River. *Hydrology and Earth System Sciences*, 24(3), 1145-
781 1157.
- 782 Liu, J., Song, X., Yuan, G., Sun, X., & Yang, L. (2014). Stable isotopic compositions of
783 precipitation in China. *Tellus Series B-Chemical and Physical Meteorology*, 66.
784 doi:10.3402/tellusb.v66.22567
- 785 Liu S. (2012). The second glacier inventory dataset of China (version 1.0) (2006-2011) [Data
786 set]. National Tibetan Plateau Data Center. Accessed 2020-01-01 from
787 <https://doi.org/10.3972/glacier.001.2013.db>.
- 788 Liu, Z., Tian, L., Yao, T., Gong, T., Yin, C., & Yu, W. (2007). Temporal and spatial variations
789 of delta O-18 in precipitation of the Yarlung Zangbo River Basin. *Journal of Geographical*
790 *Sciences*, 17(3), 317-326. doi:10.1007/s11442-007-0317-1
- 791 Lutz, A. F., Immerzeel, W. W., Shrestha, A. B., & Bierkens, M. F. P. (2014). Consistent increase
792 in High Asia's runoff due to increasing glacier melt and precipitation. *Nature Climate*

793 Change, 4(7), 587-592. doi:10.1038/nclimate2237

794 Masood, M., Yeh, P. J. F., Hanasaki, N., & Takeuchi, K. (2015). Model study of the impacts of
795 future climate change on the hydrology of Ganges–Brahmaputra–Meghna basin.
796 Hydrology and Earth System Sciences, 19(2), 747-770. doi:10.5194/hess-19-747-2015

797 McDonnell, J. J. , & Beven, K. . (2014). Debates—the future of hydrological sciences: a
798 (common) path forward? a call to action aimed at understanding velocities, celerities and
799 residence time distributions of the headwater hydrograph. Water Resources Research,
800 50(6).

801 McGuire, K. J., Weiler, M., & McDonnell, J. J. (2007). Integrating tracer experiments with
802 modeling to assess runoff processes and water transit times. Advances in Water Resources,
803 30(4), 824-837.

804 Myneni, R., Knyazikhin, Y., Park, T. (2015). MOD15A2H MODIS/Terra Leaf Area
805 Index/FPAR 8-Day L4 Global 500m SIN Grid V006 [Data set]. NASA EOSDIS Land
806 Processes DAAC. Accessed 2020-01-01 from
807 <https://doi.org/10.5067/MODIS/MOD15A2H.006>

808 Nan, Y., Tian, L., He, Z., Tian, F., & Shao, L. (2021). The value of water isotope data on
809 improving process understanding in a glacierized catchment on the Tibetan Plateau.
810 Hydrology and Earth System Sciences, 25(6), 3653-3673.

811 Noone, D., & Sturm, C. (2010). Comprehensive Dynamical Models of Global and Regional
812 Water Isotope Distributions.

813 Pu, T., Wang, K., Kong, Y., Shi, X., Kang, S., Huang, Y., . . . Cuntz, M. (2020). Observing and
814 Modeling the Isotopic Evolution of Snow Meltwater on the Southeastern Tibetan Plateau.
815 Water Resources Research, 56(9). doi:10.1029/2019wr026423

816 Rai, S. P., Singh, D., Jacob, N., Rawat, Y. S., & Arora, M. (2019). Identifying contribution of
817 snowmelt and glacier melt to the Bhagirathi River (Upper Ganga) near snout of the
818 Gangotri Glacier using environmental isotopes. Catena, 173, 339-351.

819 Reggiani, P., Hassanizadeh, S. M., Sivapalan, M., & Gray, W. G. (1999). A unifying framework
820 for watershed thermodynamics: constitutive relationships. Advances in Water Resources,
821 23(1), 15-39.

822 Schaner, N., Voisin, N., Nijssen, B., & Lettenmaier, D. P. (2012). The contribution of glacier

823 melt to streamflow. *Environmental Research Letters*, 7(3). doi:10.1088/1748-
824 9326/7/3/034029

825 Son, K., & Sivapalan, M. (2007). Improving model structure and reducing parameter
826 uncertainty in conceptual water balance models through the use of auxiliary data. *Water*
827 *Resources Research*, 43(1). doi:10.1029/2006wr005032

828 Stadnyk, T. A., Delavau, C., Kouwen, N., & Edwards, T. W. D. (2013). Towards hydrological
829 model calibration and validation: simulation of stable water isotopes using the
830 isoWATFLOOD model. *Hydrological Processes*, 27(25), 3791-3810.
831 doi:10.1002/hyp.9695

832 Sturm, C., Hoffmann, G., & Langmann, B. (2007). Simulation of the stable water isotopes in
833 precipitation over South America: Comparing regional to global circulation models.
834 *Journal of Climate*, 20(15), 3730-3750. doi:10.1175/jcli4194.1

835 Sturm, K., Hoffmann, G., Langmann, B., & Stichler, W. (2005). Simulation of delta O-18 in
836 precipitation by the regional circulation model REMOiso. *Hydrological Processes*, 19(17),
837 3425-3444. doi:10.1002/hyp.5979

838 Su, F., Zhang, L., Ou, T., Chen, D., Yao, T., Tong, K., & Qi, Y. (2016). Hydrological response
839 to future climate changes for the major upstream river basins in the Tibetan Plateau. *Global*
840 *and Planetary Change*, 136, 82-95. doi:10.1016/j.gloplacha.2015.10.012

841 Tian, F., Hu, H., Lei, Z., & Sivapalan, M. (2006). Extension of the Representative Elementary
842 Watershed approach for cold regions via explicit treatment of energy related processes.
843 *Hydrology and Earth System Sciences*, 10(5), 619-644. doi:10.5194/hess-10-619-2006

844 Tian, F., Hu, H., & Lei, Z. (2008). Thermodynamic watershed hydrological model: Constitutive
845 relationship. *Science in China Series E: Technological Sciences*, 51(9), 1353-1369.

846 Tian, F., Xu, R., Nan, Y., Li, K., & He, Z. (2020). Quantification of runoff components in the
847 Yarlung Tsangpo River using a distributed hydrological model. *Advances in Water*
848 *Science*, 31(3), 324-336.

849 Wang, C., Dong, Z., Qin, X., Zhang, J., Du, W., & Wu, J. (2016). Glacier meltwater runoff
850 process analysis using δD and $\delta^{18}O$ isotope and chemistry at the remote Laohugou
851 glacier basin in western Qilian Mountains, China. *Journal of Geographical Sciences*, 26(6),
852 722-734.

- 853 Wang, X., Zhang, X., Zhang, W., Zhang, X., & Luo, Z. (2017). Comparison on Spatial
854 Distribution of Hydrogen and Oxygen Stable Isotope GCM Simulation in Global
855 Precipitation. *Advance in Earth Sciences*, 32(9), 983-995.
- 856 Wolfe, B. B., Karst-Riddoch, T. L., Hall, R. I., Edwards, T. W. D., English, M. C., Palmini,
857 R., . . . Vardy, S. R. (2007). Classification of hydrological regimes of northern floodplain
858 basins (Peace -Athabasca Delta, Canada) from analysis of stable isotopes (δ O-18,
859 δ H-2) and water chemistry. *Hydrological Processes*, 21(2), 151-168.
860 doi:10.1002/hyp.6229
- 861 Xi, X. (2014). A Review of Water Isotopes in Atmospheric General Circulation Models: Recent
862 Advances and Future Prospects. *International Journal of Atmospheric Sciences*, 2014, 1-
863 16. doi:10.1155/2014/250920
- 864 Xu, M., Kang, S., Wang, X., Pepin, N., & Wu, H. (2019). Understanding changes in the water
865 budget driven by climate change in cryospheric-dominated watershed of the northeast
866 Tibetan Plateau, China. *Hydrological processes*, 33(7), 1040-1058.
- 867 Xu, R., Hu, H., Tian, F., Li, C., & Khan, M. Y. A. (2019). Projected climate change impacts on
868 future streamflow of the Yarlung Tsangpo-Brahmaputra River. *Global and Planetary
869 Change*, 175, 144-159. doi:10.1016/j.gloplacha.2019.01.012
- 870 Xu, R., Tian, F., Yang, L., Hu, H., Lu, H., & Hou, A. (2017). Ground validation of GPM IMERG
871 and TRMM 3B42V7 rainfall products over southern Tibetan Plateau based on a high-
872 density rain gauge network. *Journal of Geophysical Research: Atmospheres*, 122(2), 910-
873 924. doi:10.1002/2016jd025418
- 874 Yang, K., He, J., Tang, W., Qin, J., & Cheng, C. C. K. (2010). On downward shortwave and
875 longwave radiations over high altitude regions: Observation and modeling in the Tibetan
876 Plateau. *Agricultural and Forest Meteorology*, 150(1), 38-46.
877 doi:10.1016/j.agrformet.2009.08.004
- 878 Yao, T., Masson-Delmotte, V., Gao, J., Yu, W., Yang, X., Risi, C., . . . Hou, S. (2013). A review
879 of climatic controls on δ 18O in precipitation over the Tibetan Plateau: Observations and
880 simulations. *Reviews of Geophysics*, 51(4), 525-548. doi:10.1002/rog.20023
- 881 Yao, Y., Zheng, C., Andrews, C. B., Scanlon, B. R., Kuang, X., Zeng, Z., ... & Li, G. (2021).
882 Role of Groundwater in Sustaining Northern Himalayan Rivers. *Geophysical Research
883 Letters*, 48(10), e2020GL092354.

- 884 Yong, B., Wang, C. Y., Chen, J., Chen, J., Barry, D. A., Wang, T., & Li, L. (2021). Missing water
885 from the Qiangtang Basin on the Tibetan Plateau. *Geology*.
- 886 Yoshimura, K., Kanamitsu, M., Noone, D., & Oki, T. (2008). Historical isotope simulation
887 using Reanalysis atmospheric data. *Journal of Geophysical Research*, 113(D19).
888 doi:10.1029/2008jd010074
- 889 Zhang, F., Liu, J., Gong, T., & Wang, H. (2006a). Hydrological Regime of the Karuxung
890 Watershed in North Himalayas. *Acta Geographica Sinica*, 61(11), 1141-1148.
- 891 Zhang, F., Zhang, H., Hagen, S. C., Ye, M., Wang, D., Gui, D., . . . Liu, J. (2015). Snow cover
892 and runoff modelling in a high mountain catchment with scarce data: effects of
893 temperature and precipitation parameters. *Hydrological Processes*, 29(1), 52-65.
894 doi:10.1002/hyp.10125
- 895 Zhang, L., Su, F., Yang, D., Hao, Z., & Tong, K. (2013). Discharge regime and simulation for
896 the upstream of major rivers over Tibetan Plateau. *Journal of Geophysical Research:
897 Atmospheres*, 118(15), 8500-8518. doi:10.1002/jgrd.50665
- 898 Zhang, Y., Liu, S., & Ding, Y. (2006b). Spatial variation of degree-day factors on the observed
899 glaciers in western China. *ACTA GEOGRAPHICA SINICA-CHINESE EDITION*-, 61(1),
900 89.
- 901 Zhao, L., Xiao, H., Zhou, M., Cheng, G., Wang, L., Yin, L., & Ren, J. (2012). Factors
902 controlling spatial and seasonal distributions of precipitation d18O in China. *Hydrological
903 Processes*, 26(1), 143-152. doi:10.1002/hyp.8118
- 904

905 **List of figures**

906 **Figure 1.** Location and topography of (a) Tibetan Plateau, (b) Yarlung Tsangpo River basin and
907 (c) Karuxung catchment.

908 **Figure 2.** The scatter diagrams between original/corrected isoGSM and measured isotope data
909 in YTR basin (subfigures a and b) and KR catchment (subfigures c and d)

910 **Figure 3.** Temporal variations of precipitation $\delta^{18}\text{O}$ derived from measured and isoGSM data
911 in YTR basin (subfigure a) and KR catchment (subfigure b)

912 **Figure 4.** Comparisons of the amount weighted averages of precipitation $\delta^{18}\text{O}$ on 63 REWs in
913 the YTR basin by longitude (a) and elevation (b).

914 **Figure 5.** Spatial distribution of average precipitation isotope composition obtained by (a)
915 interpolated measurement data and (b) corrected isoGSM.

916 **Figure 6.** Uncertainty ranges of discharge (Nuxia station) and SCA simulations in YTR basin
917 during calibration and validation periods produced by the behavioral parameter sets of the dual-
918 objective (subfigure a and b), interpolation-forced triple-objective (subfigure c and d), and
919 isoGSM-forced triple-objective (subfigure e and f) calibration variants. The discharge data is
920 hidden for the data security policy.

921 **Figure 7.** Uncertainty ranges of stream water $\delta^{18}\text{O}$ simulations at four stations in 2005 produced
922 by the behavioral parameter sets of the dual-objective (a), interpolation-forced triple-objective
923 (b), and isoGSM-forced triple-objective (c) calibration variants.

924 **Figure 8.** Uncertainty ranges of discharge simulations at Yangcun and Nugesha stations
925 produced by the behavioral parameter sets of the dual-objective (subfigure a and b),
926 interpolation-forced triple-objective (subfigure c and d), and isoGSM-forced triple-objective
927 (subfigure e and f) calibration variants.

928 **Figure 9.** Uncertainty ranges of discharge and SCA simulations in KR catchment during
929 calibration and validation periods produced by the behavioral parameter sets of the dual-
930 objective (subfigure a and b), interpolation-forced triple-objective (subfigure c and d), and
931 isoGSM-forced triple-objective (subfigure e and f) calibration variants.

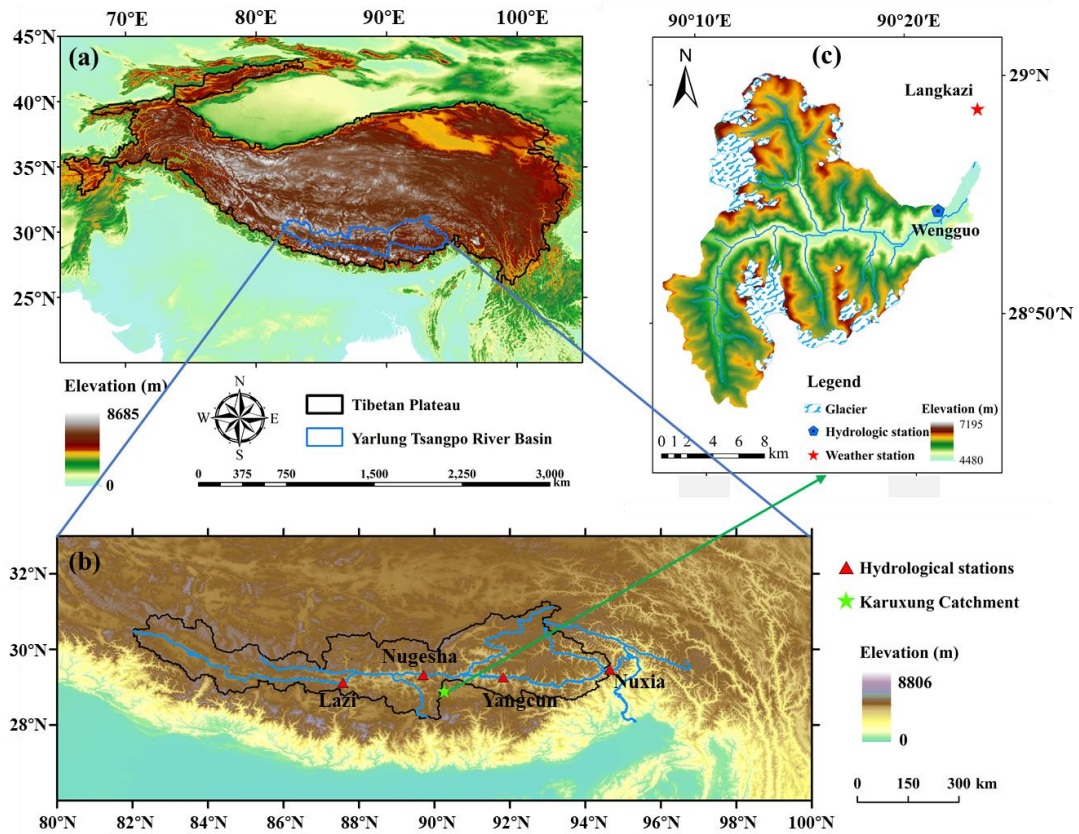
932 **Figure 10.** Uncertainty ranges of stream water $\delta^{18}\text{O}$ simulations in KR catchment during
933 calibration and validation periods produced by the behavioral parameter sets of the dual-
934 objective (a), interpolation-forced triple-objective (b), and isoGSM-forced triple-objective (c)
935 calibration variants.

936 **Figure 11.** Average proportion and corresponding uncertainty ranges of different water sources
937 in the annual water input for runoff generation estimated by different calibration variants in (a)
938 YTR and (b) KR catchments.

939 **Figure 12.** The relationships between (a) MAE_{iso} and NSE_{dis} , (b) NSE_{dis} and glacier melt
940 contribution and (c) MAE_{iso} and glacier melt contribution.

941

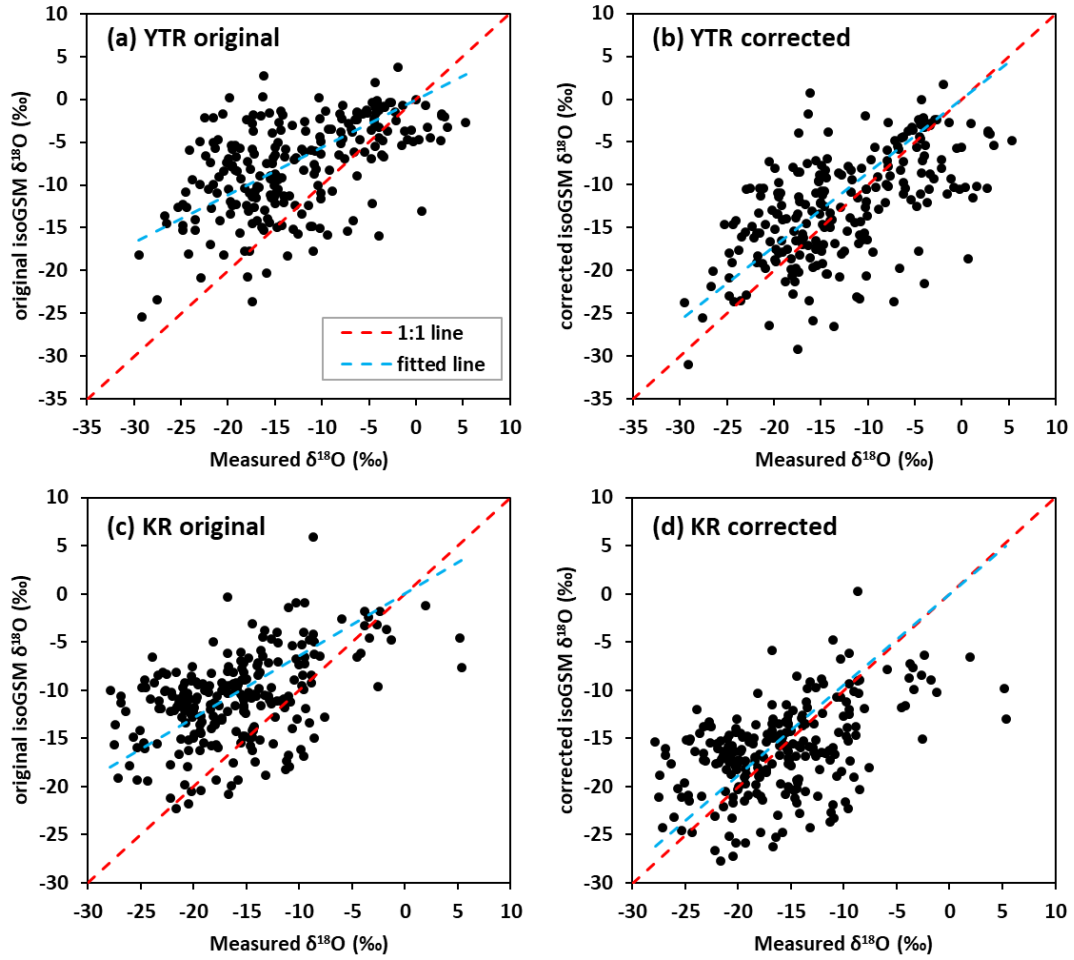
942



943

944 **Figure 1.** Location and topography of (a) Tibetan Plateau, (b) Yarlung Tsangpo River basin and
 945 (c) Karuxung catchment

946

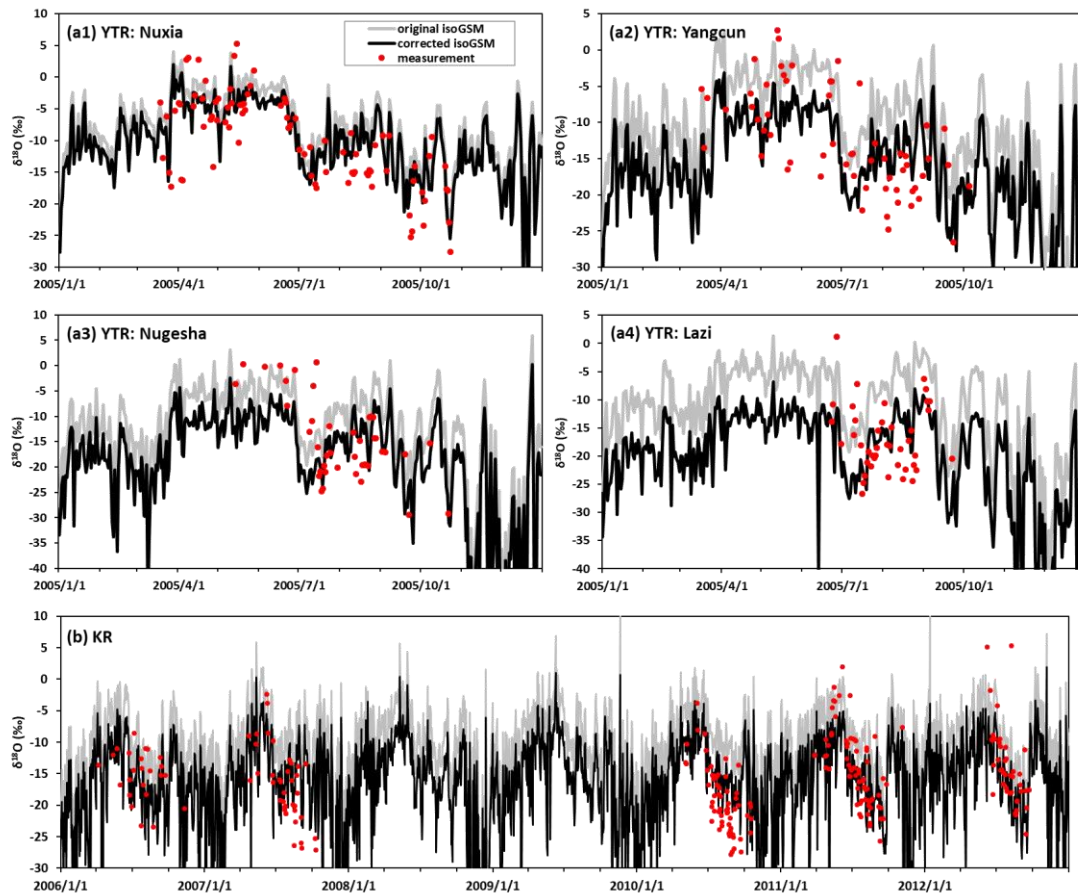


947

948 **Figure 2.** The scatter diagrams between original/corrected isoGSM and measured isotope data

949 in YTR basin (subfigures a and b) and KR catchment (subfigures c and d).

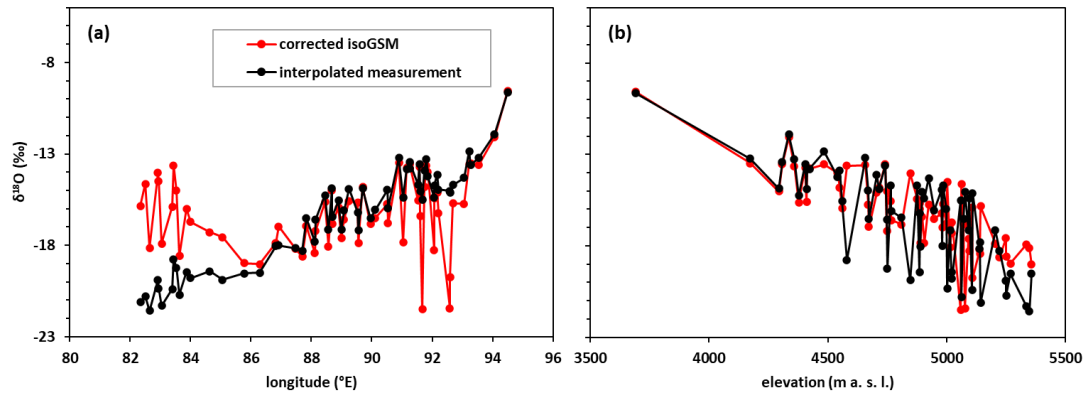
950



951

952 **Figure 3.** Temporal variations of precipitation $\delta^{18}\text{O}$ derived from measured and isoGSM data
 953 in YTR basin (subfigure a) and KR catchment (subfigure b).

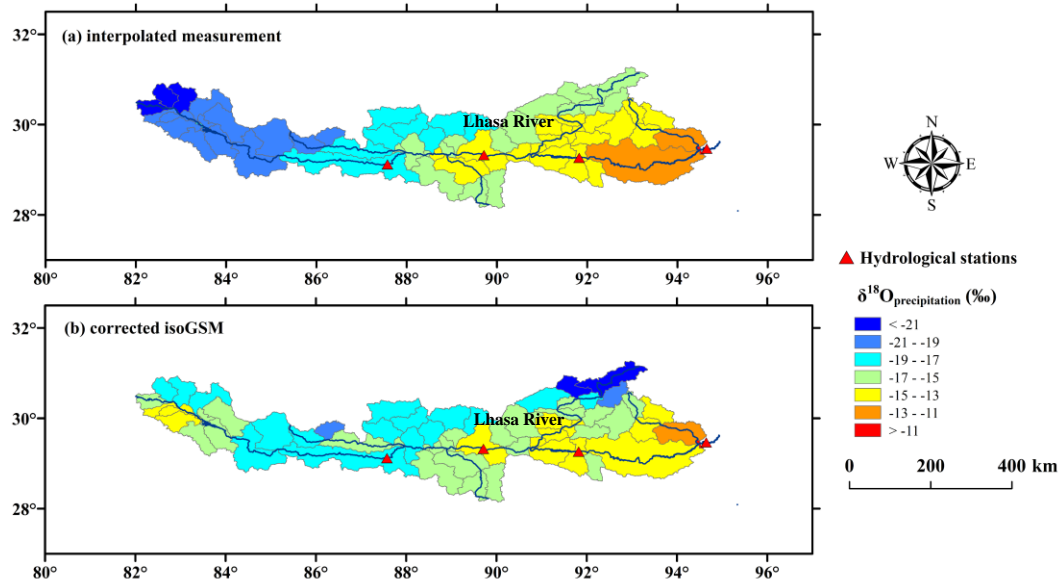
954



955

956 **Figure 4.** Comparisons of the amount weighted averages of precipitation $\delta^{18}\text{O}$ on 63 REWs in
 957 the YTR basin by longitude (a) and elevation (b).

958

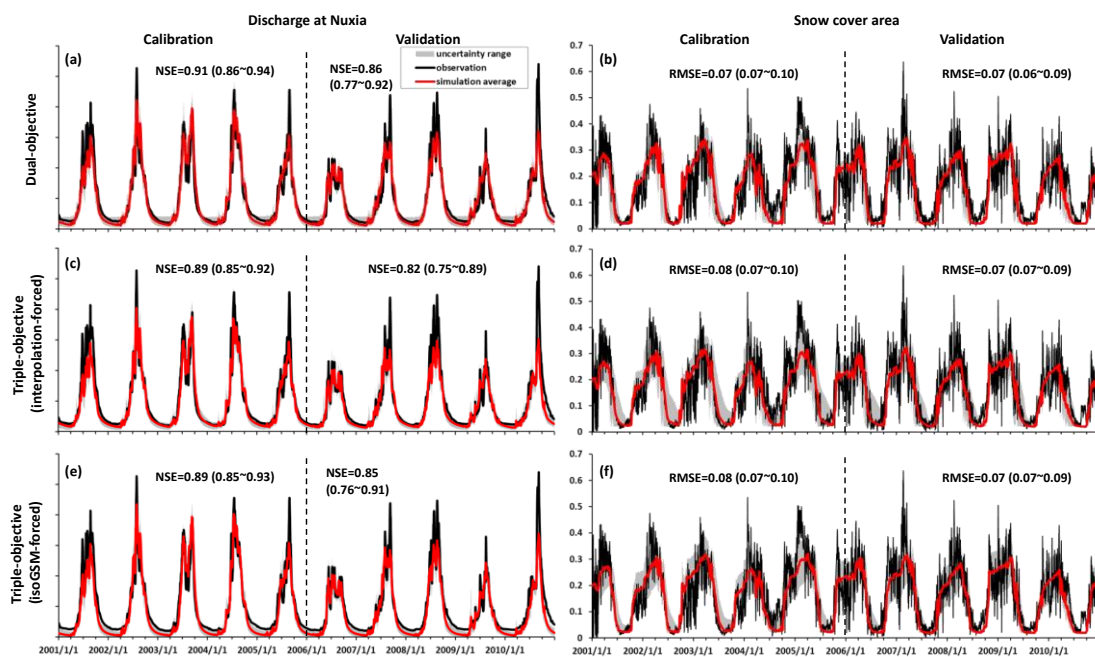


959
 960
 961
 962

Figure 5. Spatial distribution of average precipitation isotope composition obtained by (a) interpolated measurement data and (b) corrected isoGSM.

963

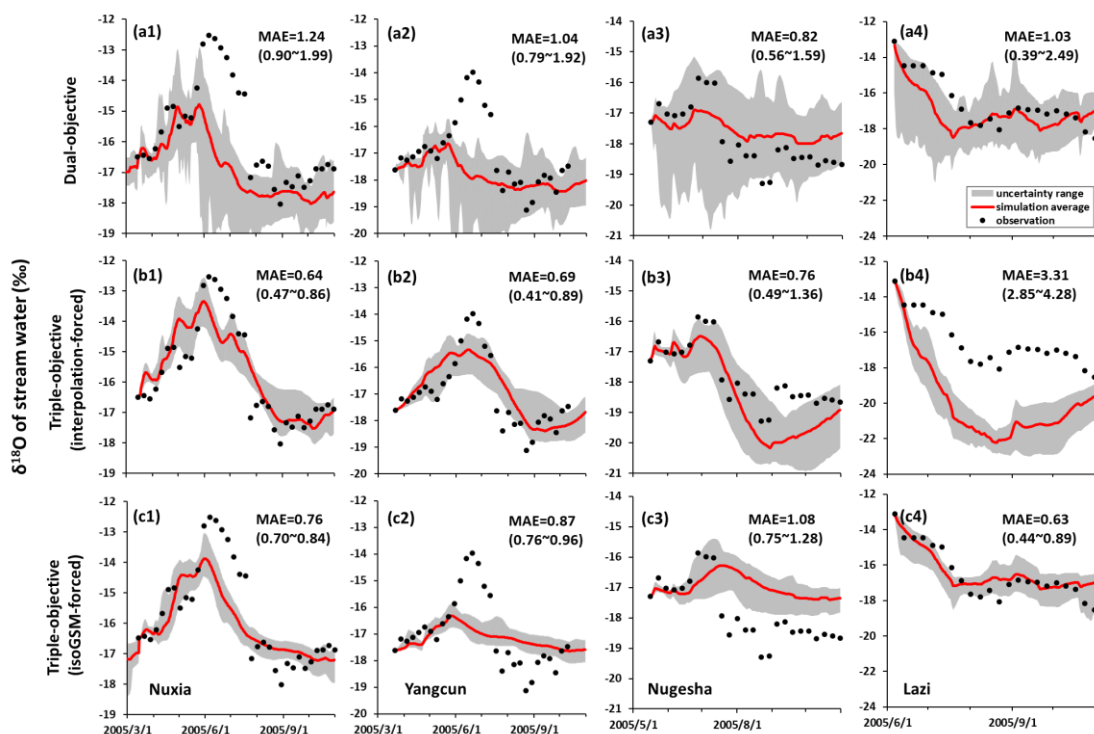
964



965

966 **Figure 6.** Uncertainty ranges of discharge (Nuxia station) and SCA simulations in YTR basin
967 during calibration and validation periods produced by the behavioral parameter sets of the dual-
968 objective (subfigure a and b), interpolation-forced triple-objective (subfigure c and d), and
969 isoGSM-forced triple-objective (subfigure e and f) calibration variants. The scale of discharge
970 axis is hidden due to data security policy.

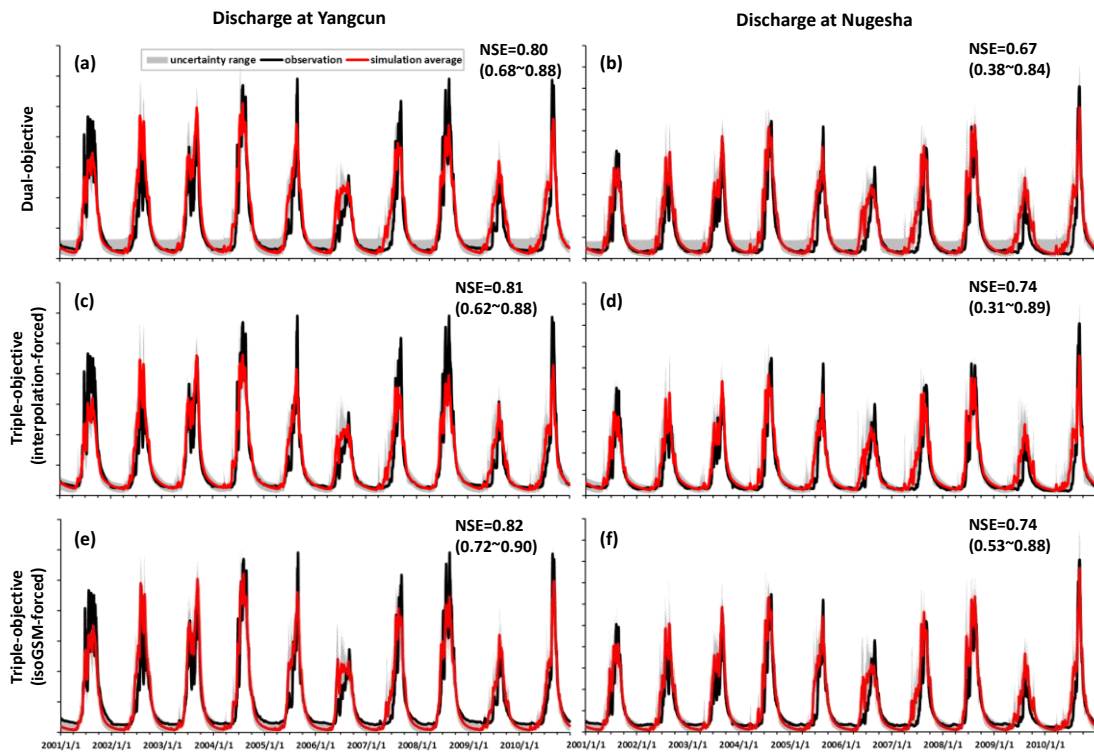
971



973

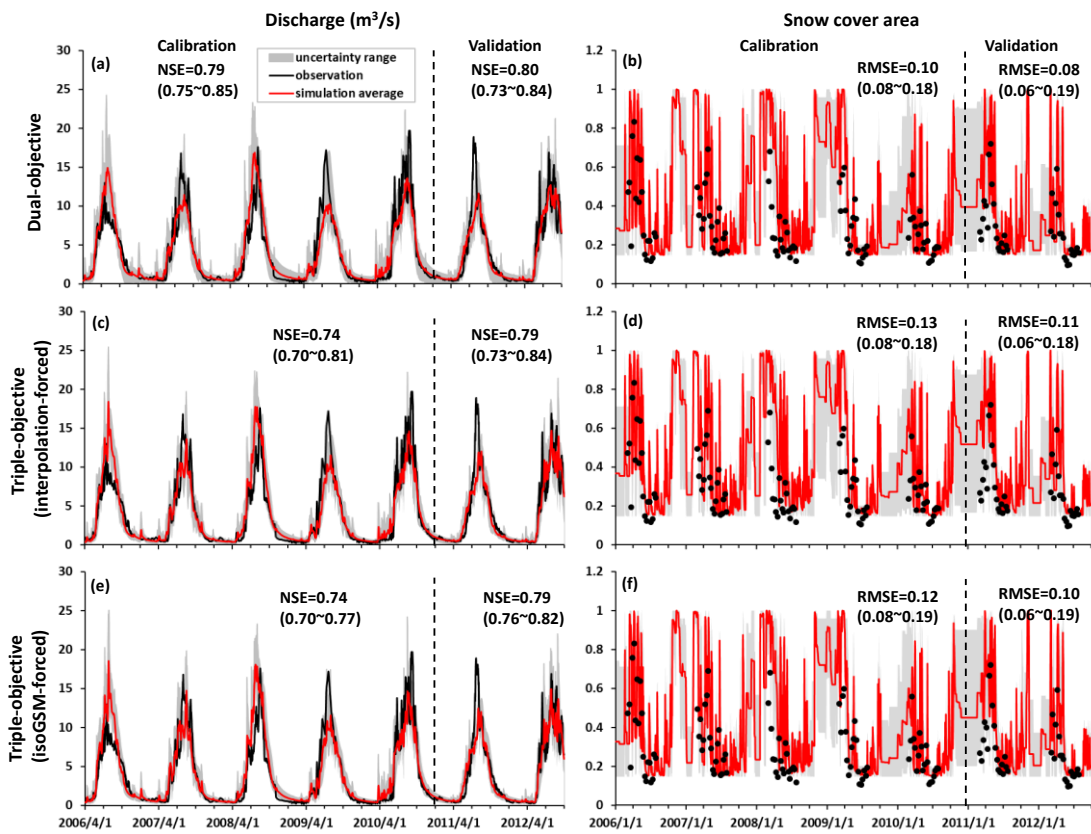
974 **Figure 7.** Uncertainty ranges of stream water $\delta^{18}\text{O}$ simulations at four stations in 2005 produced
 975 by the behavioral parameter sets of the dual-objective (a), interpolation-forced triple-objective
 976 (b), and isoGSM-forced triple-objective (c) calibration variants.

977



979

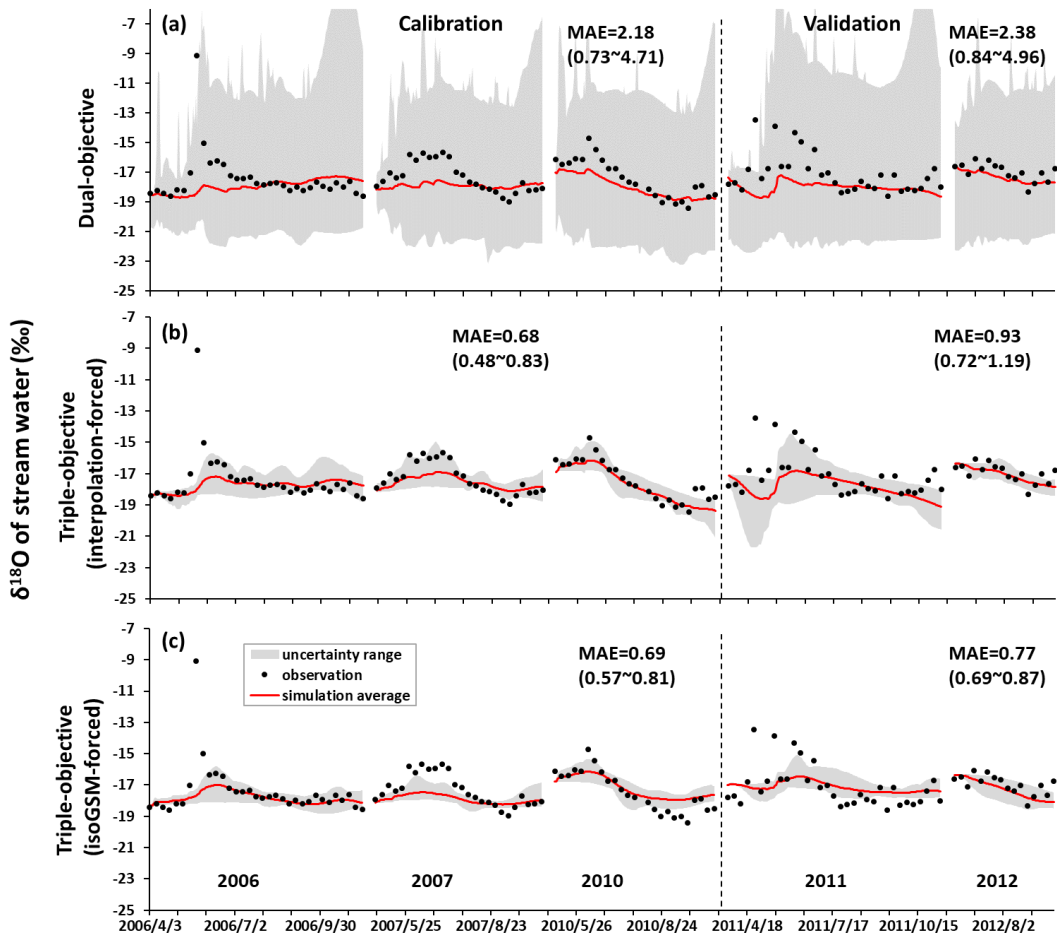
980 **Figure 8.** Uncertainty ranges of discharge simulations at Yangcun and Nugesha stations
 981 produced by the behavioral parameter sets of the dual-objective (subfigure a and b),
 982 interpolation-forced triple-objective (subfigure c and d), and isoGSM-forced triple-objective
 983 (subfigure e and f) calibration variants.
 984



986

987 **Figure 9.** Uncertainty ranges of discharge and SCA simulations in KR catchment during
 988 calibration and validation periods produced by the behavioral parameter sets of the dual-
 989 objective (subfigure a and b), interpolation-forced triple-objective (subfigure c and d), and
 990 isoGSM-forced triple-objective (subfigure e and f) calibration variants.

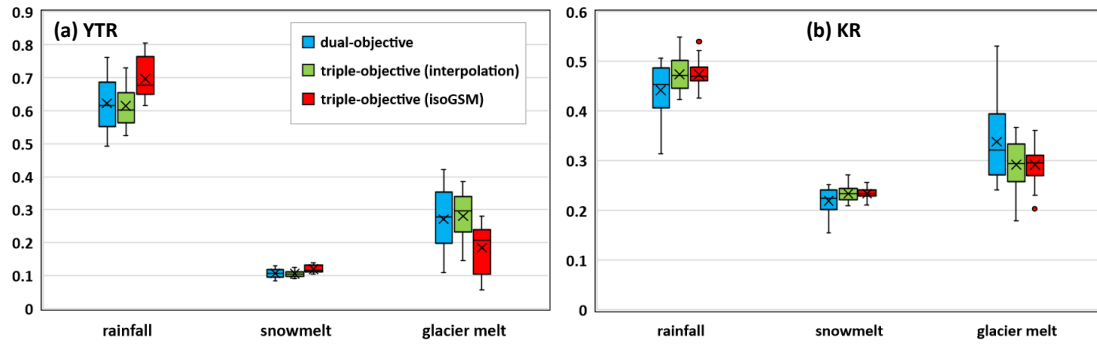
991



993

994 **Figure 10.** Uncertainty ranges of stream water $\delta^{18}\text{O}$ simulations in KR catchment during
 995 calibration and validation periods produced by the behavioral parameter sets of the dual-
 996 objective (a), interpolation-forced triple-objective (b), and isoGSM-forced triple-objective (c)
 997 calibration variants.

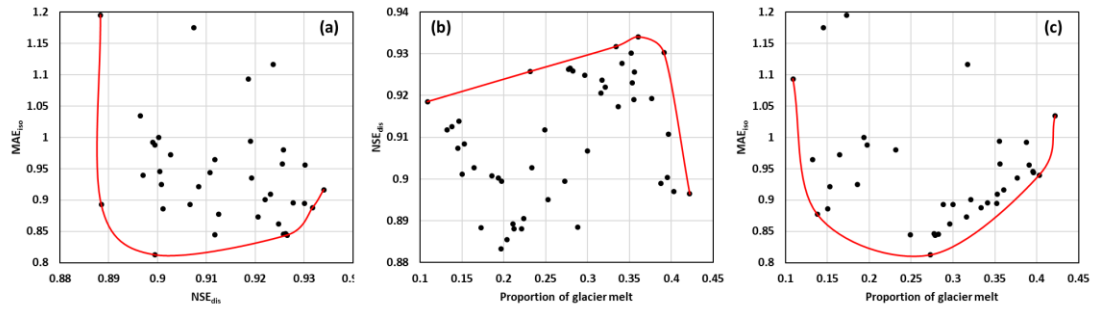
998



999

1000 **Figure 11.** Average proportion and corresponding uncertainty ranges of different water sources
 1001 in the annual water input for runoff generation estimated by different calibration variants in (a)
 1002 YTR and (b) KR catchments.

1003



1004

1005 **Figure 12.** The relationships between (a) MAE_{iso} and NSE_{dis}, (b) NSE_{dis} and glacier melt

1006 contribution and (c) MAE_{iso} and glacier melt contribution.

1007

1008

1009

1010 **List of tables**

1011 **Table 1.** Characteristics of precipitation and stream water samples in YTR and KR
1012 catchments.

1013 **Table 2.** Calibrated parameters of the THREW-t model.

1014 **Table 3.** Comparisons of the model performance in YTR basin produced by different calibration
1015 variants.

1016 **Table 4.** Comparisons of the model performance in KR catchment produced by different
1017 calibration variants.

1018 **Table 5.** Average proportions of water sources in the annual and seasonal water inputs for
1019 runoff generation in YTR basin.

1020 **Table 6.** Average proportions of water sources in the annual and seasonal water inputs for
1021 runoff generation in KR catchment.

1022

1023

Table 1. Characteristics of precipitation and stream water samples in YTR and KR catchments.

Catchment (Station)	Year	Period Dd/mm to dd/mm	Precipitation sample number	Stream sample number
YTR (Nuxia)		14/03 to 23/10	86	34
YTR (Yangcun)	2005	17/03 to 05/10	59	30
YTR (Nugesha)		14/05 to 22/10	45	25
YTR (Lazi)		06/06 to 22/09	42	22
		2006	04/06 to 11/11	24
	2007	23/04 to 09/10	39	25
KR (Wengguo)	2010	05/05 to 18/10	63	23
	2011	28/03 to 06/11	69	32
	2012	16/06 to 22/09	42	14

1024

1025

Table 2. Calibrated parameters of the THREW-t model

Symbol	Unit	Physical descriptions	Range
nt	-	Manning roughness coefficient for hillslope	0-0.2
WM	cm	Tension water storage capacity, used in Xinanjiang model (Zhao, 1992) to calculate saturation area	0-10
B	-	Shape coefficient used in Xinanjiang model to calculate saturation area	0-1
KKA	-	Coefficient to calculate subsurface runoff in $Rg=KKD \cdot S \cdot K^S_S \cdot (y_s/Z)^{KKA}$, where S is the topographic slope, K^S_S is the saturated hydraulic conductivity, y_s is the depth of saturated groundwater, Z is the total soil depth	0-6
KKD	-	See description for KKA	0-0.5
T_0	°C	Temperature threshold above which snow and glacier melt	-5-5
DDF_N	mm/°C/day	Degree day factor for snow	0-10
DDF_G	mm/°C/day	Degree day factor for glacier	0-10
$C1$	-	Coefficient to calculate the runoff concentration process using Muskingum method: $O_2=C_1 \cdot I_1+C_2 \cdot I_2+C_3 \cdot O_1+C_4 \cdot Q_{lat}$, where I_1 and O_1 is the inflow and outflow at prior step, I_2 and O_2 is the inflow and outflow at current step, Q_{lat} is lateral flow of the river channel, $C_3=1-C_1-C_2$, $C_4=C_1+C_2$	0-1
$C2$	-	See description for $C1$	0-1

1026

1027 **Table 3.** Comparisons of the model performance in YTR basin produced by different calibration
 1028 variants.

calibration variant	behavioral ratio ^a	period /station ^b	NSE_{dis} ^{c,d}	RMSE_{SCA}	MAE_{iso}
Dual-objective	0.98	calibration	0.91 (0.86-0.93)	0.07 (0.07-0.10)	1.24 (0.90-1.99)
		validation	0.86 (0.77-0.92)	0.07 (0.06-0.09)	0.96 (0.75~1.97)
Triple-objective (measurement)	0.64	calibration	0.89 (0.85-0.92)	0.08 (0.07-0.10)	0.64 (0.47-0.86)
		validation	0.82 (0.75-0.89)	0.07 (0.07-0.09)	1.46 (1.17-1.93)
Triple-objective (isoGSM)	0.82	calibration	0.89 (0.85-0.93)	0.08 (0.07-0.10)	0.76 (0.70-0.84)
		validation	0.85 (0.76-0.91)	0.07 (0.07-0.09)	0.87 (0.76-1.04)

1029 a: Behavioral ratio represents the ratio of behavioral parameter set number to the run time of pySOT
 1030 program.

1031 b: “Period” for discharge and SCA simulation, and “station” for isotope simulation.

1032 c: Bracketed values represent the minimal and maximal values produced by the behavioral parameter
 1033 sets.

1034 d: NSE_{dis} is calculated based on the simulated and observed streamflow at Nuxia station

1035

1036 **Table 4.** Comparisons of the model performance in KR catchment produced by different
 1037 calibration variants.

calibration variant	behavioral ratio	period	NSE_{dis}	RMSE_{SCA}	MAE_{iso}
Dual-objective	0.78	calibration	0.79 (0.75-0.85)	0.10 (0.08-0.18)	2.18 (0.73-4.71)
		validation	0.80 (0.73-0.84)	0.08 (0.06-0.19)	2.38 (0.84-4.96)
Triple-objective (measurement)	0.13	calibration	0.74 (0.70-0.81)	0.13 (0.08-0.18)	0.68 (0.48-0.83)
		validation	0.79 (0.73-0.84)	0.11 (0.06-0.18)	0.93 (0.72-1.19)
Triple-objective (isoGSM)	0.12	calibration	0.74 (0.70-0.77)	0.12 (0.08-0.19)	0.69 (0.57-0.81)
		validation	0.79 (0.76-0.82)	0.10 (0.06-0.19)	0.77 (0.69-0.87)

1038

1039 **Table 5.** Average proportions of water sources in the annual and seasonal water inputs for
 1040 runoff generation in YTR basin.

Season	Water source ^a	Dual-objective	Triple-objective (measurement)	Triple-objective (isoGSM)
Annual	Rainfall	62.2	61.4	69.6
	Snow melt	10.7	10.6	12.0
	Glacier melt	27.1	28.0	18.4
	Uncertainty	11.4	8.6	8.9
Spring	Rainfall	35.4	36.8	44.2
	Snow melt	42.9	39.7	43.8
	Glacier melt	21.7	23.5	12.0
	Uncertainty	13.4	12.8	11.8
Summer	Rainfall	69.8	68.2	74.5
	Snow melt	3.4	4.4	6.4
	Glacier melt	26.8	27.4	19.1
	Uncertainty	10.2	7.9	8.7
Autumn	Rainfall	63.1	61.9	76.1
	Snow melt	3.5	3.5	2.7
	Glacier melt	33.5	34.7	22.0
	Uncertainty	16.1	12.8	13.3
Winter	Rainfall	11.9	12.8	30.8
	Snow melt	70.1	65.8	61.7
	Glacier melt	18.0	21.4	7.5
	Uncertainty	19.7	20.6	30.8

1041 a: The uncertainty of the contribution is defined as $E = \sqrt{E_R^2 + E_N^2 + E_G^2}$, where E_R , E_N and E_G
 1042 represent the standard deviations of the contributions of the water sources produced by the corresponding
 1043 behavioral parameter sets. Subscripts of R , N and G represent rainfall, snow meltwater and glacier
 1044 meltwater, respectively.

1045

1046 **Table 6.** Average proportions of water sources in the annual and seasonal water inputs for
 1047 runoff generation in KR catchment.

Season	Water source	Dual-objective	Triple-objective (measurement)	Triple-objective (isoGSM)
Annual	Rainfall	44.2	47.4	47.4
	Snow melt	22.0	23.4	23.4
	Glacier melt	33.8	29.2	29.2
	Uncertainty	9.4	6.2	4.7
Spring	Rainfall	4.1	4.5	4.5
	Snow melt	56.3	61.6	60.9
	Glacier melt	39.5	33.9	34.6
	Uncertainty	13.7	14.2	12.0
Summer	Rainfall	53.5	56.6	56.9
	Snow melt	14.0	15.2	15.1
	Glacier melt	32.4	28.2	28.0
	Uncertainty	9.7	5.1	3.9
Autumn	Rainfall	30.9	35.0	34.3
	Snow melt	33.9	35.3	35.5
	Glacier melt	35.1	29.7	30.3
	Uncertainty	11.2	11.0	9.6
Winter	Rainfall	0	0	0
	Snow melt	55.3	63.3	58.9
	Glacier melt	44.7	36.7	41.1
	Uncertainty	22.3	31.5	29.2

1048